

Molecular gas distribution perpendicular to the Galactic plane

YANG SU,¹ JI YANG,^{1,2} QING-ZENG YAN,¹ SHAOBO ZHANG,¹ HONGCHI WANG,^{1,2} YAN SUN,¹
ZHIWEI CHEN,¹ CHEN WANG,¹ XIN ZHOU,¹ XUEPENG CHEN,^{1,2} ZHIBO JIANG,¹ AND MIN WANG¹

¹*Purple Mountain Observatory and Key Laboratory of Radio Astronomy, Chinese Academy of Sciences, Nanjing
210023, China*

²*School of Astronomy and Space Science, University of Science and Technology of China, 96 Jinzhai Road, Hefei
230026, China*

ABSTRACT

We use the ~ 370 square degrees data from the MWISP CO survey to study the vertical distribution of the molecular clouds (MCs) toward the tangent points in the region of $l = [+16^\circ, +52^\circ]$ and $|b| < 5^\circ.1$. We find that the molecular disk consists of two components with a layer thickness (FWHM) of ~ 85 pc and ~ 280 pc, respectively. In the inner Galaxy, the molecular mass in the thin disk is dominant, while the molecular mass traced by the discrete MCs with weak CO emission in the thick disk is probably $\lesssim 10\%$ of the whole molecular disk. For the CO gas in the thick disk, we identified 1055 high- z MCs that are $\gtrsim 100$ pc from the Galactic plane. However, only a few samples (i.e., 32 MCs or 3%) are located in the $|z| \gtrsim 360$ pc region. Typically, the discrete MCs of the thick-disk population have a median peak temperature of 2.1 K, a median velocity dispersion of 0.8 km s^{-1} , and a median effective radius of 2.5 pc. Assuming a constant value of $X_{\text{CO}} = 2 \times 10^{20} \text{ cm}^{-2} (\text{K km s}^{-1})^{-1}$, the median surface density of these MCs is $6.8 M_\odot \text{ pc}^{-2}$, indicating very faint CO emission for the high- z gas. The cloud-cloud velocity dispersion is $4.9 \pm 1.3 \text{ km s}^{-1}$ and a linear variation with a slope of $\sim -0.4 \text{ km s}^{-1} \text{ kpc}^{-1}$ is obtained in the region of $R_{\text{GC}} = 2.2\text{--}6.4 \text{ kpc}$. Assuming that these clouds are supported by their turbulent motions against the gravitational pull of the disk, a model of $\rho_0(R) = 1.28 M_\odot \text{ pc}^{-3} e^{-\frac{R}{3.2 \text{ kpc}}}$ can be used to describe the distribution of the total mass density in the Galactic midplane.

Keywords: Interstellar medium (847); Molecular clouds (1072); Surveys (1671); Milky Way disk (1050); Interstellar dynamics (839); Stellar-interstellar interactions (1576)

1. INTRODUCTION

CO is a good tracer of the molecular gas in the interstellar medium (ISM). Many CO surveys (e.g., see Heyer & Dame 2015; Schuller et al.

2021) have been undertaken to study the physical properties and the distribution of molecular clouds (MCs) in the Milky Way. Astronomers often use these large-scale CO data to investigate the Galactic structure, e.g., the spiral arms, the molecular gas disk, the scale height of the gas plane, and some spe-

cial large-scale regions such as the central molecular zone, etc (refer to the good summaries in Combes 1991, Dame et al. 2001, and Heyer & Dame 2015; also see some recent works based on the large-scale CO data such as Benedettini et al. 2020; Dame & Thaddeus 2008, 2011; Eden et al. 2020; Rigby et al. 2016; Schuller et al. 2017, 2021; Sofue et al. 2019; Torii et al. 2019).

The Milky Way Imaging Scroll Painting (MWISP) project is an ongoing large-scale, unbiased, and high-quality CO survey toward the northern Galactic plane (e.g., see more details in Su et al. 2019). The MWISP survey offers an excellent opportunity to improve our understanding of the Galactic structure. Based on the rich CO data set of the new survey, actually, many results on the Galactic structure are also present (e.g., see the different arm structures in Du et al. 2016, 2017; Su et al. 2016; Sun et al. 2015, 2017, 2020). Generally, the molecular gas in the inner Galaxy is well confined to the plane, while the gas at large Galactocentric distances (e.g., $R_{GC} \gtrsim 10$ kpc in Su et al. 2016) often displays the flaring and warping structures.

Additionally, the new CO data reveal that the considerable molecular gas is located in the region away from the $b = 0^\circ$ plane in the inner Galaxy because of the larger latitude coverage of $b = [-5^\circ.1, 5^\circ.1]$ in the MWISP survey (Su et al. 2019). A similar thick molecular disk was investigated both in the Milky Way (Dame & Thaddeus 1994; Malhotra 1994a) and other galaxies (e.g., NGC 891 by Garcia-Burillo et al. 1992 and M51 by Pety et al. 2013). Following the study by Dame & Thaddeus (1994), we have confirmed that the CO disk in the inner Galactic plane is composed of two components, a well-known thin disk with an FWHM of 88.5 pc and an additional faint thick CO disk with an FWHM of 276.8 pc. However, the properties and distributions of the molecular gas in the Galactic thick

disk have not been studied in detail due to the lack of high-quality large-scale data and large MC samples.

In this paper, we focus on the vertical distribution of the molecular gas near the tangent points by using the accumulated CO data from the MWISP. Benefiting from the good angular resolution, excellent sensitivity, and high dynamic range of the MWISP survey, we identified over 1000 MCs far from the Galactic plane to trace the thick CO disk in the region of $l = 16^\circ\text{--}52^\circ$ and $|b| \lesssim 5^\circ.1$. The properties, distributions, and origins of these MCs far from the Galactic plane (hereafter the high- z MCs) are investigated accordingly.

The paper is organized as follows. In Section 2, we briefly describe the CO observations and data processing. Section 3 shows the results and discussions on the CO distribution perpendicular to the Galactic disk and the MCs far from the midplane. The distribution of the total midplane mass density as a function of the Galactocentric distance is also investigated in the section based on the estimations of the cloud-cloud velocity dispersion and the scale height of the CO gas. Finally, we summarize our results in Section 4.

2. CO DATA

We employed the ~ 370 deg² CO data (i.e., $l = 16^\circ\text{--}52^\circ$ and $|b| \lesssim 5^\circ.1$) from the MWISP project (see the details in Su et al. 2019) to study the vertical distribution of the molecular gas. Briefly, the ¹²CO, ¹³CO, and C¹⁸O ($J=1\text{--}0$) lines were simultaneously observed with the full-sampling On-The-Fly mapping (see Sun et al. 2018) by using the nine-beam Superconducting Spectroscopic Array Receiver system (Shan et al. 2012). The spatial and spectral resolutions of the CO data are $\sim 50''$ and ~ 0.2 km s⁻¹, respectively. The quality of the CO data is good, and the first-order (or linear) baseline was fit for all spectra. After removing the bad channels and abnormal

spectra, the reduced 3D data cubes (position-position-velocity, hereafter PPV) with a uniform grid spacing of $30''$ have typical rms noise levels of ~ 0.5 K for ^{12}CO at a channel width of 0.16 km s^{-1} and ~ 0.3 K for ^{13}CO (C^{18}O) at 0.17 km s^{-1} , respectively.

3. RESULTS AND DISCUSSIONS

3.1. Terminal Velocities from the MWISP CO Data

Figure 1 displays the schematic view of the molecular gas discussed in this paper. The red belt with a length of ~ 5.1 kpc shows the region of the tangent-point MCs between $l = 16^\circ$ and $l = 52^\circ$. The blue circle indicates the approximate radius of the end of the bar (i.e., the 3 kpc ring structure). The gas emission inside of the circle drops sharply. Assuming a circular motion of MCs in the Milky Way, we can easily obtain the distances ($d = R_0 \times \cos l$) and Galactocentric distances ($R_{\text{GC}} = R_0 \times \sin l$) for the MCs at the terminal velocity. Here, the value of the Sun's distance to the Galactic center, R_0 , is taken to be 8.15 kpc (see the recent work by Reid et al. 2019).

The CO emission near the tangent points is mainly concentrated in the region of $|b| \lesssim 1.5^\circ$ (e.g., see Figure 6 in Su et al. 2019). Considering the large-scale distribution of the CO gas near the tangent points, we divide the whole region into 36 subregions to determine the corresponding terminal velocity in the range of $l = 16^\circ - 52^\circ$. Each subregion is centered at $b=0^\circ$ and has an area of 3 deg^2 , i.e., $\Delta l = 1^\circ$ and $b = [-1.5, 1.5]$. The average spectra of these subregions were extracted to search for the CO peak emission at the most positive velocity, i.e., the tangent velocity, $V_{\text{tan}}(l)$, for each sampled Galactic longitude. At the tangent point, the typical value of the average peak ^{12}CO temperature of each subregion is selected to be $T_{\text{peak}12} \gtrsim 0.5$ K for $l = 22^\circ - 52^\circ$ and $T_{\text{peak}12} \gtrsim 0.2$ K for $l = 16^\circ - 22^\circ$. That is, the

smaller features (and thus the MCs with very weak CO emission) are ignored because we only focus on the ensemble of the large-scale molecular gas near the tangent points in each subregion. These smaller features with somewhat larger V_{LSR} are probably due to local variations of the environment (i.e., the abnormal velocities from star-forming activities, e.g., H II regions, star winds, supernova remnants, etc.) and non-circular motions from other effects near the tangent points. For blended and confused CO emission, the combined ^{13}CO line is also used to define the CO peak emission at the most positive velocity (i.e., $V_{\text{tan}}(l)$ at $T_{\text{peak}13} \gtrsim 0.2$ K).

The above approach to define the terminal velocity can avoid the effects of the contaminated emission from the wing of a component and non-circular motions from some smaller molecular features (e.g., the redshift velocity from the perturbed gas near the tangent points). We plot the determined curve of the terminal velocity on the longitude-velocity diagram (i.e., the LV map) by interpolating for the MWISP CO data in the region of $l = [16^\circ, 52^\circ]$ (see the red line in Figure 2). We find that our result is consistent with previous CO studies (e.g., see Clemens 1985; Malhotra 1994b).

For further comparisons of the tangent-point features at the most positive velocity, we also overlaid the terminal velocity curves from the HI observations (the gold lines; McClure-Griffiths & Dickey 2016) and the trigonometric parallaxes of high-mass star-forming regions (the purple line; see the A5 model from Reid et al. 2019) on the CO LV map, respectively. Generally, for the discussed region, the l - V_{tan} trend is very similar between our CO result and the HI result, although our CO terminal velocity is systematically smaller (several km s^{-1}) than that of the HI observations. Actually, we find that the HI terminal-velocity curve is nearly around the outer layer of the CO emission at the most extreme velocity

(see the thick golden line in Figure 2). The difference between the CO result and the HI result is probably due to (1) the different properties of the two tracers, and (2) the different methods used in studies.

On the other hand, models based on different tracers also display somewhat differences in calculating the terminal velocity at different Galactic longitudes (e.g., the thin golden line vs. the purple line in Figure 2). Further investigations are helpful to clarify these issues by combining the HI and CO data in a larger longitude range. In this paper, we tentatively use the MWISP CO observations to trace the terminal velocity (see the red line in Figure 2) for the subsequent analysis. As discussed below, the slight variation of the terminal velocity does not change our analysis and result considerably.

3.2. Thin and Thick Molecular Disks

Using the terminal velocity curve determined in Section 3.1, we can investigate the vertical distribution of the molecular gas at the tangent points. We made the integrated ^{12}CO emission in the velocity range of $V(l) \gtrsim V_{\text{tan}}(l) - 7 \text{ km s}^{-1}$ to trace the molecular gas at the most positive velocity (Figure 3). Some large-scale structures near the tangent points are labeled on the map (e.g., refer to Bland-Hawthorn & Gerhard 2016; Reid et al. 2016). The value of 7 km s^{-1} was adopted to take into account the cloud-cloud velocity dispersion of the molecular gas near the tangent points (e.g., see Malhotra 1994b). Actually, this value is roughly consistent with the maximum cloud-cloud velocity dispersion measured from the tangent-point MCs based on the MWISP CO observations (Section 3.4).

Based on the ^{12}CO emission near the most positive velocity (Figure 3), we find that molecular gas is mainly concentrated around the plane in the inner Galaxy (e.g., $|b| \lesssim 1^\circ$ or $|z| \lesssim 100 \text{ pc}$). The whole region from $l = [+16^\circ, +52^\circ]$ is divided into six ranges of longitude to investigate the vertical distribution of

the molecular gas. For a certain region, CO emission at the same distance from the Galactic plane of $b = 0^\circ$ (i.e., $z = R_{\text{GC}} \cos(l) \tan(b)$) is integrated assuming the gas is located at the tangent points. Along the direction perpendicular to the Galactic plane, the total intensity of the CO emission with a bin of 5 pc is then fitted by using a Gaussian function, i.e., $I(z)/I_{\text{peak}} = \exp(-\frac{(z-z_0)^2}{2\sigma_z^2})$. Here, z_0 and σ_z (i.e., the thickness $\text{FWHM} = 2.355\sigma_z$) in units of parsec is the mean value and the standard deviation of the vertical distribution of the CO emission, respectively. Note that the CO gas outside the $|z| \gtrsim 100\text{--}150 \text{ pc}$ region does not affect our single-Gaussian fitting because the high- z emission is very weak in the total CO intensity near the tangent points.

The best fit of the vertical distribution of the ^{12}CO emission is shown in Figure 4, while the result of the ^{13}CO emission is also shown for comparison. Obviously, the z_0 values from the ^{12}CO emission agree well with those from the ^{13}CO emission, indicating that the molecular gas traced by the optically thick and thin lines is concentrated toward the midplane. We find that the mean thickness of the ^{12}CO disk is roughly 94 pc between $l = 22^\circ$ and $l = 52^\circ$, which is larger than the value of $\sim 60 \text{ pc}$ in the region of $l = 16^\circ - 22^\circ$. On the whole, the narrow Gaussian component represents well the thin molecular gas disk that is dominated by the enhanced CO emission near the Galactic midplane.

Meanwhile, there are amounts of CO gas located far from the Galactic plane (Figure 3). To investigate the distribution of the gas far from the plane, we use the mean intensity in each 5 pc bin to reveal the weak CO emission. That is, we use the mean intensity in an effective area (i.e., $I_{\text{total}}/\sqrt{N_{\text{pixel}}}$ for pixels of $I_{\text{CO}} \gtrsim 3I_{\text{rms}}$) to investigate the distribution of the CO gas in the disk. Obviously, this processing nearly does not affect the distribution of the gas in the thin

disk because of the strong CO emission there. However, it can highlight the distribution of the weak CO emission in the high- z region because only pixels with $I_{\text{CO}} \gtrsim 3I_{\text{rms}}$ are accounted for. By adopting the known values of z_0 and σ_z for the thin CO disk (i.e., the narrow Gaussian component from Figure 4), we can easily fit another broad Gaussian component for the thick CO disk (Figure 5).

As a result, a mean FWHM of ~ 256 pc (excluding the region of $l = 16^\circ - 22^\circ$) can well describe the thick molecular gas disk. It is worth mentioning that the gas distribution of the thick disk is not symmetric with respect to the thin CO disk in some regions. Then the fitted z_0 values of the thick disk are not always consistent with those from the thin CO disk (e.g., see the enhanced CO emission at $z \lesssim -100$ pc in the longitude range of $22^\circ - 28^\circ$ in Figure 5). Actually, we also note that there are lots of atomic clouds below the Galactic plane in a similar region (e.g., see the $l = 22^\circ - 31^\circ$ and $b \lesssim -2^\circ$ region in Figure 11). This feature probably indicates that the gas of the thick disk is probably decoupled from the thin gas layer in some regions.

Similarly, we also measured the mean thickness of the molecular disk in the whole range of $l = 16^\circ - 52^\circ$ (the upper panels in Figure 6) and $l = 22^\circ - 52^\circ$ (the lower panels in Figure 6) by using the best fit of the two Gaussian components. The thickness of the thin and thick CO disk is roughly 107 pc and 301 pc, respectively. Both of the two values from the wider longitude region are $\sim 15\%$ larger than the results from the smaller subregions of $\Delta l = 6^\circ$ (i.e., 107 pc vs. 94 pc for the thin CO disk and 301 pc vs. 256 pc for the thick CO disk).

We further investigate the variation of the thin disk over the Galactic longitude. Based on the measurements of the 30 subregions with $\Delta l = 1^\circ$, the mean thickness of the thin CO layer (excluding $l = 16 - 22^\circ$) is ~ 85 pc (see

the right panel in Figure 7), which is slightly smaller than values of $\sim 94-107$ pc from Figures 4 and 6. We note that the mean thickness of the thin CO disk remains almost unchanged in the region of $l \sim 22 - 52^\circ$, while the thickness of the $l \sim 16 - 22^\circ$ region is considerably smaller (see the right panel in Figure 7). According to Figure 3, we also note that the CO emission in $l = 16^\circ$ and $l = 22^\circ$ is relatively weak with respect to other regions near the tangent points. We speculated that it is probably due to the effect of the dynamical perturbation within the 3 kpc ring.

The larger values of the thickness of the CO layer from Figure 6 can be attributed to the variation of z_0 at different Galactic longitudes, which will widen the thickness of the gas disk by fitting data from the larger longitude range. Indeed, we find that z_0 changes from negative values at $l \sim 37 - 52^\circ$ to positive values at $l \sim 16 - 37^\circ$ (see the left panel in Figure 7). As discussed in Heyer & Dame (2015), other methods probably yield a higher value for the CO layer thickness due to corrugations in the inner Galactic disk (e.g., FWHM $\sim 100-120$ pc in Bronfman et al. 1988; Clemens et al. 1988; Sanders et al. 1984; Nakanishi & Sofue 2006).

We also check our fitting by using the integrated CO emission from somewhat different velocity ranges, e.g., $V(l) \gtrsim V_{\text{tan}}(l) - 4 \text{ km s}^{-1}$ and $V(l) \gtrsim V_{\text{tan}}(l) - 10 \text{ km s}^{-1}$. The resultant fittings are not changed significantly. To recapitulate briefly, our recommended thickness of the thin CO layer of ~ 85 pc is in agreement with the value of ~ 90 pc from Malhotra (1994b), and the thickness of the thick CO layer is about 260–300 pc, which is also consistent with previous studies (e.g., Dame & Thaddeus 1994). The thick molecular disk revealed by the faint CO emission is about three times as wide as the well-known central thin CO layer. The thickness of the thick CO layer is also comparable in width to the central HI layer (e.g., 250–270 pc in

Dickey & Lockman 1990; Lockman & Gehman 1991).

Moreover, the thickness of the thick CO layer from the MWISP survey is just between ~ 190 pc for the diffuse H₂ gas and ~ 320 pc for the diffuse HI+warm ionized medium (WIM) gas by considering $R_0 = 8.15$ kpc (see the discussions of the bright/faint diffuse C II-without-CO emission in Velusamy & Langer 2014). These results show that a considerable amount of molecular gas in the CO-faint H₂ clouds can be revealed by the high-resolution and high-sensitivity CO survey. In the following section, we will investigate the distributions and properties of the CO-faint molecular gas based on the newly identified high- z MCs near the tangent points.

3.3. MCs Far from the Galactic Plane

3.3.1. Identification of the High- z MCs

MCs far from the Galactic plane are identified by using the density-based spatial clustering of applications with noise (DBSCAN¹) clustering algorithm. Full details can be found in Yan et al. (2020), and a brief description of the method is presented below.

First, the 3D PPV data cubes in the velocity interval of 40–160 km s⁻¹ are smoothed to 0.5 km s⁻¹ to decrease the random noise fluctuations in the velocity axis. In the PPV space, the minimum number of neighborhood voxels (MinPts) is set to 16 and the minimum cutoff on the data is $2 \times \text{rms}$ (i.e., the lowest level to surround the 3D structure). The peak brightness temperature (T_{peak}) is $\geq 5 \times \text{rms}$ (here, the rms is ~ 0.3 K for the smoothed channel width of 0.5 km s⁻¹ for ¹²CO) to control the quality of the selected samples. Second, the projection area on the spatial scale has at least 4 pixels (\sim one beam), and the minimum channel number in the velocity axis is considered to be ≥ 3 to reduce

striping artifacts and other uncertainties in the whole data. These criteria are helpful to obtain as much of the emission as possible and to avoid the contamination of the noise in the 3D data, leading to weak but true signals for the large-scale CO data to be picked up. Broad criteria (e.g., MinPts=12 and/or $T_{\text{peak}} = 3 \times \text{rms}$) will increase the number of the MC sample; however, there is usually a large uncertainty for the true MC identification due to the confusion with the noise fluctuations.

Finally, MCs far from the Galactic plane are selected based on the further criteria of $V_{\text{MC}} \gtrsim V_{\text{tan}}(l) - 7 \text{ km s}^{-1}$ and $z_{\text{MC}}(l, b, v) \leq z_0(l) - 3\sigma_z(l)$ or $z_{\text{MC}}(l, b, v) \geq z_0(l) + 3\sigma_z(l)$. Here, $z_0(l)$ and $\sigma_z(l)$ can be obtained based on the best fit of the $z_0(l)$ - l and $\sigma_z(l)$ - l relations from the thin CO disk (see the measurements and the fitting lines in Figure 7). That is, MCs in the thin CO disk are excluded due to their concentrated distribution in the region of $b \sim 0^\circ$, i.e., $z_0(l) - 3\sigma_z(l) < z_{\text{MC}}(\text{thin disk}) < z_0(l) + 3\sigma_z(l)$.

In total, 1055 samples near the tangent points were identified as the MCs far from the Galactic plane between $l = 16^\circ$ and $l = 52^\circ$ based on the MWISP ¹²CO data. The MCs, which have weak CO emission, are relatively isolated with respect to the molecular gas near the Galactic midplane. Table 1 lists the parameters of each MC, i.e, (1) the ID of the identified MCs, arranged from the low Galactic longitude; (2) and (3) the MC's Galactic coordinates (l and b); (4) the MC's LSR velocity (V_{LSR}); (5) the MC's one-dimensional velocity dispersion (σ_v); (6) the MC's peak emission (T_{peak}); (7) the MC's area; (8) the MC's distance obtained from the tangent points, i.e, $d = R_0 \times \cos(l)$; (9) the MC's z scale defined as $z = d \times \tan(b)$; (10) the MC's mass estimated from the CO-to-H₂ conversion factor method, $X_{\text{CO}} = 2 \times 10^{20} \text{ cm}^{-2} (\text{K km s}^{-1})^{-1}$ (e.g., Dame et al. 2001; Bolatto et al. 2013); and (11) the MC's virial

¹ https://scikit-learn.org/stable/auto_examples/cluster/plot_dbscan.html

parameter $\alpha = \frac{M_{\text{virial}}}{M_{\text{Xfactor}}} = \frac{5\sigma_v^2 R}{GM_{\text{Xfactor}}}$, where R is the radius of the MC and G the gravitational constant. We can easily use MWISP Glll.lll±bb.bbb±vvv.vv to name an MC identified from the CO survey.

3.3.2. *Properties and Statistics of the High- z MCs*

For the molecular gas far from the Galactic plane, Figure 8 displays the vertical distribution of the 1055 MCs, which can be fitted by a Gaussian function with $z_0 = -15.9$ pc and $\sigma_z = 113.1$ pc. The standard deviation of the vertical distribution is ~ 113 pc (and thus the FWHM of ~ 270 pc) for the gas layer traced by the ensemble of the high- z MCs, which is roughly similar to the measurement from the CO emission in the thick molecular gas layer (Section 3.1).

Importantly, the excellent agreement of the vertical distribution of these discrete MCs with that of the thick CO disk emission proposed by Dame & Thaddeus (1994) confirms their claim that the high- z emission they observed is not substantially contaminated by sidelobe pickup from the central disk. Therefore, our results based on the large-scale, high-resolution, and high-sensitivity data demonstrate convincingly that the thick molecular gas disk is indeed an important component in the inner Galaxy. The thick molecular disk is composed of many discrete MCs with small size and low mass (see below).

Figure 9 shows the properties of the MCs. Typically, these MCs have $T_{\text{peak}} \sim 1\text{--}4$ K, with the median value of 2.1 K, indicating very faint CO emission (i.e., $\sim 4\text{--}10 M_{\odot}\text{pc}^{-2}$ assuming a constant CO-to- H_2 conversion factor) for these small MCs. The effective radii of these MCs are $0'.8\text{--}1'.6$ ($\sim 1\text{--}2$ beam size), indicating that the MCs at the tangent are unresolved because of the spatial resolution limit of the data, i.e., 1–4 pc at distances of 5–8 kpc. We find that a truncated power-law function with a slope

of $\gamma = -1.74$ (i.e., $N(M > M_0) \propto M^{\gamma+1}$ for the cloud’s mass range of $\sim 120\text{--}8000 M_{\odot}$) can describe the mass distribution of the high- z MCs, which is consistent to $\gamma \sim -1.7$ observed for the MCs in the Milky Way (e.g., Roman-Duval et al. 2010; Heyer & Dame 2015; Rice et al. 2016; Colombo et al. 2019). The velocity dispersion (σ_v) of the high- z MCs is roughly 0.8 km s^{-1} , leading to $\alpha \gtrsim 10$ for the most of CO clouds.

Obviously, the lower limit of T_{peak} , radius, and surface density is related to (1) the limited sensitivity and spatial resolution of the current CO survey, and (2) the selection criterion of the MCs used in Section 3.3.1. We mention that some clouds with weak CO emission ($T_{\text{peak}} \lesssim 1$ K) and/or smaller sizes (radius $\lesssim 1'$) are missed due to the observational limit of the MWISP survey. Therefore, a substantial amount of the fainter CO emission (e.g., $\lesssim 1 \text{ K km s}^{-1}$ or $M \lesssim 100\text{--}150 M_{\odot}$) could probably be unveiled by higher-sensitivity CO surveys.

The cloud-cloud velocity dispersion (σ_{cc}) of these high- z MCs can be estimated from the samples with $V_{\text{LSR}} \gtrsim V_{\text{tan}}$. Obviously, the estimation of σ_{cc} depends on the definition of the $l - V_{\text{tan}}$ relation. By taking into account the slight variation of the tangent velocity, we find that the cloud-cloud dispersion varies from $4.4 \pm 1.6 \text{ km s}^{-1}$ for $V_{\text{LSR}} \gtrsim V_{\text{tan}}$ to $5.6 \pm 1.5 \text{ km s}^{-1}$ for $V_{\text{LSR}} \gtrsim V_{\text{tan}} - 7 \text{ km s}^{-1}$ with the 1° bin samples in the $l = [+16^\circ, +52^\circ]$ region. The cloud-cloud velocity dispersion only changes a little with the variation of the selected tangent velocity. On the other hand, the estimated σ_{cc} of these MCs is comparable to the measured cloud-cloud velocity dispersion of the total MC samples near the Galactic plane (see Section 3.4 and other works, e.g., Stark & Brand 1989; Malhotra 1994b).

Interestingly, the low σ_{cc} of the high- z MCs in the Milky Way is different from the finding that

a potential thick gas disk may have a high velocity dispersion for galaxies (e.g., $\sigma_{cc} \sim 12 \text{ km s}^{-1}$ for the thick molecular gas disk with extended/diffuse CO emission; [Caldú-Primo et al. 2013](#)). As discussed in [Krumholz et al. \(2018\)](#), the high mass transport rates and star formation rates can lead to the high velocity dispersions of the gas in galaxies. Briefly, we summarized all of the physical properties for the high- z MCs in Table 2.

As seen in Figure 10, the MCs are mainly concentrated in regions of $l = 22^\circ - 30^\circ$ (i.e., $R_{GC}=3.1-4.1 \text{ kpc}$) and $l = 43^\circ - 52^\circ$ (i.e., $R_{GC}=5.6-6.4 \text{ kpc}$). A smaller concentration is between the two peak distributions (i.e., see the $l = 32^\circ - 38^\circ$ or $R_{GC}=4.3-5.0 \text{ kpc}$ region in Figure 10). We suggest that the large-scale structures (i.e., the Norma arm, the Aquila Spur toward the tip of the Galactic bar, and the Carina-Sagittarius arm; see Figures 1 and 3; refer to [Bland-Hawthorn & Gerhard 2016](#); [Reid et al. 2016](#)) near the tangent points are probably responsible for the three peaks at the longitude distribution (or R_{GC}) of the enhanced high- z MCs. Interestingly, the scatter of σ_{cc} is relatively larger in the region of $l \sim 22^\circ - 38^\circ$ (Figure 12), which indicates that the Galactic bar may have an important impact on the dynamics and distribution of the gas in the inner Galaxy.

We also find that the high- z HI gas is abundant in the region of $l \sim 20^\circ - 30^\circ$ ([Ford et al. 2010](#)), although the vertical distribution of the high- z HI clouds is much wider than that of the CO clouds (i.e., $300 \text{ pc} \lesssim |z_{\text{HI cloud}}| \lesssim 1700 \text{ pc}$ vs. $100 \text{ pc} \lesssim |z_{\text{CO cloud}}| \lesssim 250 \text{ pc}$ in the 90% range). Figure 11 shows the comparison between the high- z MWISP CO clouds and the GASS HI clouds in the range of $l=[+17^\circ.1,+34^\circ.2]$ and $b=[+5^\circ.1,-5^\circ.1]$. We note that some HI samples in [Ford et al. \(2010\)](#) are very likely related to our CO clouds, e.g., (1) the GASS HI cloud: ($18^\circ.72, -2^\circ.00, 126.1 \text{ km s}^{-1}$) ver-

sus the MWISP CO cloud: ($18^\circ.805, -1^\circ.937, 131.27 \text{ km s}^{-1}$); (2) the GASS HI cloud: ($19^\circ.19, +2^\circ.06, 136.3 \text{ km s}^{-1}$) versus the MWISP CO cloud: ($19^\circ.213, +2^\circ.134, 137.38 \text{ km s}^{-1}$); (3) the GASS HI cloud: ($19^\circ.61, +4^\circ.43, 138.0 \text{ km s}^{-1}$) versus the MWISP CO cloud: ($19^\circ.512, +4^\circ.377, 137.84 \text{ km s}^{-1}$), etc. The spatial and kinematical relationships between the HI cloud and the CO cloud are worth exploring in more detail in future works by using the high-quality HI data (e.g., from the GALFA-HI survey; [Peek et al. 2011, 2018](#)) and MWISP CO data. Here we briefly discuss the possible origin of the high- z MCs in Section 3.3.3.

In the region of $|z - z_0| > \sigma_z$ (i.e., the region outside the $1 \times \sigma_z$ of the thick CO disk), the molecular gas mass is about $3.6 \times 10^5 M_\odot$ based on the discovered high- z MCs by adopting $z_0 = -15 \text{ pc}$ and $\sigma_z = 120 \text{ pc}$ (e.g., see Figure 8). The value is approximately 31.7% of the total mass of the thick CO disk in the 5.1 kpc long red belt (see Figure 1; including an extrapolation of the component through the full Galactic disk by assuming a Gaussian distribution). Thus, the total mass of the thick CO disk in the belt region is about $1.1 \times 10^6 M_\odot$. Adopting a mean width of 0.5 kpc for the red belt (i.e., the mean path length along the line of sight for the belt; see the model in [Lockman 1984](#)), we obtain an area of 2.55 kpc^2 (i.e., 5.1 kpc length \times 0.5 kpc width) projected on the Galactic plane. The total midplane density of the thick disk is thus $\sim 0.43 M_\odot \text{ pc}^{-2}$, leading to the volume density of $\sim 0.0014 M_\odot \text{ pc}^{-3}$ (or $\sim 0.02 \text{ H}_2 \text{ cm}^{-3}$) in the discussed region by assuming the Gaussian distribution of $\rho(z) = \rho_0 \exp(-\frac{(z-z_0)^2}{2\sigma_z^2})$. We mentioned that the estimated values are probably the lower limit due to the limited observational sensitivity and resolution of the MWISP survey (i.e., the missing molecular gas mass for the very faint CO emission and small clouds that are not involved in the calculation). In the region of $R_{GC} = 2-8.15 \text{ kpc}$, the molecular mass

of the thick CO disk is thus $\sim 8.5 \times 10^7 M_\odot$, which is about 10% of the total molecular mass in the inner Galaxy (i.e., $\sim 7.8 \times 10^8 M_\odot$ for the thin CO disk + the thick CO disk; this paper and Heyer & Dame 2015).

3.3.3. Origin of the high- z MCs

According to the vertical distribution of the high- z molecular gas (Figure 8), we find that the identified MCs are mainly concentrated in the $100 \text{ pc} \lesssim |z| \lesssim 360 \text{ pc}$ region. However, there is only a little amount of molecular gas traced by CO emission in the region of $|z| \gtrsim 360 \text{ pc}$ (i.e., 32/1055 high- z MCs). We thus suggest that these MCs with faint CO emission probably belong to the disk population. The spatial and velocity coincidence between some CO clouds and the corresponding HI clouds is very interesting. It indicates that considerable amounts of molecular gas appear to survive in the disk-halo transition region (or in the disk-halo zone close to the Galactic midplane; e.g., $100 \text{ pc} \lesssim |z| \lesssim 300 \text{ pc}$). The coexistence of molecular gas and the atomic gas in the disk-halo transition region needs to be further investigated based on the observational and theoretical studies.

Generally, the typical internal crossing time of these high- z MCs is about 3 Myr assuming the typical radius of $\sim 3 \text{ pc}$ and velocity dispersion of $\sigma_v = 0.9 \text{ km s}^{-1}$ (Figure 9). This value is roughly an order of magnitude smaller than the dynamical timescale of the moving clouds from the Galactic midplane (i.e., $t_{\text{dyn}} = \frac{z}{\sigma_{\text{cc}}} \gtrsim 24 \text{ Myr}$, where $\sigma_{\text{cc}} = 4.9 \text{ km s}^{-1}$ is the cloud-cloud velocity dispersion from Section 3.4). It indicates that the MCs' memory of their birthplace is lost, and any observed kinematical features from the line profile and spatial morphology probably represent the turbulence in the current local environment. Considering the prevalent turbulence in the ISM, the cloud will be destroyed quickly due to the Kelvin-Helmholtz

and Rayleigh-Taylor instabilities (e.g., $\lesssim 1 \text{ Myr}$ in Iwasaki et al. 2019).

On the other hand, the high virial parameter of the clouds shows that the high- z MCs are unstable unless they are confined by some external pressure. The low σ_{cc} of $\sim 5 \text{ km s}^{-1}$ and large σ_z of 260–300 pc for these high- z MCs indicate that the gravitational force of the midplane is not balanced by the gas pressure, suggesting that the ensemble of the MCs is in general out of equilibrium. All of these results show that the high- z MCs probably have short lifetimes less than several Myr (e.g., comparable to the typical internal crossing time). Indeed, if the MCs directly move from the Galactic plane to their current places, the moving velocity of the clouds should be an order of magnitude larger than that of the cloud-cloud dispersion velocity because of the short lifetime of these clouds (e.g., \lesssim several Myr). Alternatively, some of the high- z MCs are probably newborn clouds due to the rapid H_2 formation in shock interaction regions (e.g., with the high ram pressure of $\gtrsim 10^5 - 10^6 \text{ K cm}^{-3}$, see Su et al. 2018). We suggest that these MCs are transitory. The high- z molecular gas with faint CO emission is either dispersing or being assembled by some external dynamical processes (e.g., compression by shocks, cloud-cloud collision, and shear motions, etc).

Whatever the exact formation mechanism of the high- z clouds, the energetic sources near the Galactic plane may play important roles in the origin of the disk-population gas (e.g., the stellar feedback from massive stellar winds and/or supernova explosions; see the Galactic fountain models in Shapiro & Field 1976; Bregman 1980; Houck & Bregman 1990; Spitoni et al. 2008; Soler et al. 2020). Recently, di Teodoro et al. (2020) also found that the cold, dense, and high-velocity molecular gas survives in the Milky Way's nuclear wind at $\sim 600\text{--}900 \text{ pc}$ from the Galactic plane. Likewise, the interactions be-

tween the disk gas and the halo gas are probably common in the Milky Way and other galaxies due to energetic processes in the galactic plane (e.g., see the disk-halo scenario discussed in Lockman 2002; Ford et al. 2008, 2010; Putman et al. 2012).

Finally, we summarize the thickness of the inner disk revealed by the different gas tracers in Table 3. The fact that the thickness of the thick disk traced by the CO gas ($\sim 260\text{--}300$ pc in this work) and the HI(CII) gas (e.g., $\sim 250\text{--}270$ pc for HI emission and $\sim 190\text{--}320$ pc for CII emission, Dickey & Lockman 1990; Lockman & Gehman 1991; Langer et al. 2014; Velusamy & Langer 2014) is comparable may be a relevant hint to establishing a link between the formation/evolution of the high- z MCs and various physical processes. Further studies will be helpful to clarify these issues through a combination of multiwavelength data, e.g., the kinematical connection between the CO clouds and the HI clouds, possible related IR features, and/or emission from other tracers like OH 18 cm, CH 3.3 GHz lines, and $158\ \mu\text{m}$ [CII] lines, etc.

3.4. *Cloud-to-cloud Velocity Dispersion near the Tangent Points and the Total Midplane Density*

The HI and H₂ gas in the inner Galaxy ($R_{\text{GC}} = R_0 \lesssim 8.15$ kpc) is concentrated toward the thin plane due to the gravitational potential of the matter in the Galactic disk. If the pressure from magnetic fields, cosmic rays, and the radiation field is ignored, the vertical distribution of the H₂ gas is mainly determined by the total gravitating mass near the disk (i.e., stars, gas, and possible other unknown objects). Considering the balance between the turbulent pressure of the isothermal molecular gas and the gravitational force on the Galactic plane, we can obtain the formula of $\rho_0 = \frac{\sigma_{\text{cc}}^2}{4\pi G \sigma_z^2}$ for the Gaussian distribution of the gas layer (e.g., see Malhotra 1994b, 1995). Here, ρ_0 is the to-

tal density of the midplane mass, σ_{cc} is the cloud-cloud velocity dispersion, and σ_z is the scale height of the thin CO layer. We ignore the scale height of the thick CO disk due to its limited contribution to the total molecular gas mass (i.e., $\sim 3\%$ for the $|z| \gtrsim 120$ pc molecular gas).

In principle, we can estimate the midplane mass density of the Galactic disk if σ_{cc} and σ_z are obtained from observations. Figure 12 displays the distribution of σ_{cc} for all MCs near the tangent points (i.e., MCs in the thin and thick disk with $V_{\text{LSR}}(\text{MC}) \gtrsim V_{\text{tan}} - \Delta V$). Here, ΔV is simply selected as $3.9\ \text{km s}^{-1}$ (i.e., roughly three times of the scatter of σ_{cc} , which is nearly constant for the tangent MCs in the longitude range) by taking into account the tangent MCs with somewhat lower V_{LSR} . We note that the estimated value of σ_{cc} is in the range of $2.7\text{--}7.9\ \text{km s}^{-1}$ (i.e., mean value of $4.9\ \text{km s}^{-1}$ and a scatter of $1.3\ \text{km s}^{-1}$), which is close to that of the high- z MCs discussed in Section 3.3.2. The value is roughly consistent with other works based on different approaches (e.g., see Blitz et al. 1984; Clemens 1985; Stark 1984; Stark & Brand 1989; Malhotra 1994b).

Additionally, the distribution of σ_{cc} seems to display a linear variation with a slope of $\sim -0.4\ \text{km s}^{-1}\text{kpc}^{-1}$ between $R_{\text{GC}}=2.2\text{--}6.4$ kpc. It is interesting to note that the slope from the CO data is about one-half of the HI gas when the joint gravitational potential is considered (i.e., stars, HI gas, and H₂ gas near the disk; see Narayan & Jog 2002). The decrease of σ_{cc} at larger R_{GC} may be explained by a lower star formation rate in the outer part of the inner disk if σ_{cc} (i.e., the turbulence of the MCs) is regulated by the energy input via star-forming activities near the Galactic plane. On the other hand, however, it should be mentioned that the measured σ_{cc} based on our CO data also displays considerable fluctuation in different R_{GC} (see Figure 12), which is probably related to the

different localized environment. More quantitative studies are required to better understand these features.

Combining the measurements of $R_{\text{GC}}-\sigma_{\text{cc}}$ and $R_{\text{GC}}-\sigma_z$ for MCSs near the tangent points, we can obtain the distribution of the total mass density in the Galactic plane (i.e., $R_{\text{GC}}-\rho_0$ in Figure 13). The error of ρ_0 can be calculated from the fitting error of σ_z (Figure 7) and the assumed error of σ_{cc} (Figure 12). We find that an exponential-disk model of $\rho_0(R) = \rho_{\text{GC}}e^{-R/R_{\text{sl}}}$ can roughly fit the distribution of the total mass density for the $R_{\text{GC}}=2.25\text{--}6.42$ kpc region. Here, $\rho_{\text{GC}}=1.28 M_{\odot} \text{pc}^{-3}$ is the mass density at the Galactic center and $R_{\text{sl}} = 3.20$ kpc is the scale length of the disk. The mid-plane mass density at the Sun is estimated to be $\rho_0(R_0)=0.10 M_{\odot} \text{pc}^{-3}$, which agrees well with the Oort limit summarized in McKee et al. (2015). Because of the lower CO emission in the tangent points of $l \lesssim 22^\circ$ (i.e., $R_{\text{GC}} \lesssim 3$ kpc for the 3 kpc ring structure in Figure 2), we also fit the data in the $R_{\text{GC}}=3.05\text{--}6.42$ kpc region. The resultant fitting of $R_{\text{GC}}-\rho_0$ gives a similar result (see the blue line in Figure 13).

4. SUMMARY

Based on the MWISP CO data, we have performed a study of the vertical distribution of the molecular gas near the tangent points in the range of $l = 16^\circ\text{--}52^\circ$ and $|b| \lesssim 5^\circ.1$. The main results are:

1. The terminal velocity of the molecular gas, which is comparable to other observations and theoretical models, is well determined from the new MWISP CO survey toward the inner Galaxy (Figure 2).

2. We use the CO emission near the terminal velocity to trace the molecular gas distribution at the tangent points, which can avoid the distance ambiguity within the solar circle. The high-quality CO data reveal two main molecular gas features near the tangent points, including large-scale bright CO emission in the

Galactic midplane and discrete MCSs with very weak emission in relatively high- b regions (see Figure 3).

3. Based on the integrated CO intensity near the terminal velocity, we find that the model of two Gaussian components can be used to describe the vertical distribution of the molecular gas near the tangent points. The narrow one with a FWHM of ~ 85 pc is the well-known thin molecular gas disk in the inner Galaxy, while another broad component with a FWHM of $\sim 260\text{--}300$ pc probably represents the thick CO disk. For the thin CO disk, Figure 7 displays the systematic variation of the offset (z_0) and the scale height (σ_z) of the molecular gas with respect to the Galactic longitude, which is consistent with previous studies (e.g., Malhotra 1994b). For the thick CO disk, its thickness is about three times as wide as that of the well-known thin molecular gas layer, and the thickness of the thick molecular gas layer is very comparable in width to the central atomic gas layer (e.g., 250-270 pc in Dickey & Lockman 1990; Lockman & Gehman 1991).

4. For the thick CO disk, a total of 1055 high- z MCSs were identified at the tangent points in the first quadrant region of the MWISP survey. These MCSs have a median radius of 2.5 pc, a median velocity dispersion of 0.8 km s^{-1} , and a median peak temperature of 2.1 K. The mass surface brightness of the MCSs is very low, i.e., a median value of $6.8 M_{\odot}\text{pc}^{-2}$ assuming a constant CO-to- H_2 conversion factor of $2 \times 10^{20} \text{ cm}^{-2}(\text{K km s}^{-1})^{-1}$. The cloud-cloud velocity dispersion of the high- z MCSs is $4.4\text{--}5.6 \text{ km s}^{-1}$, which is similar to the value of $4.9 \pm 1.3 \text{ km s}^{-1}$ for all MCSs at the tangent points. The high virial parameter indicates that the high- z MCSs are probably short-lived objects. That is, the MCSs of the new disk population are either dispersing or being assembled by some external dynamical processes. Alternatively, some of the high- z MCSs are probably

newborn clouds in an environment of the high ram pressure. Our findings show that the thick CO disk is composed of many discrete MCs with small size and low mass (i.e., $\frac{dN}{dM} \propto M^{-1.74}$ in the MC's mass range of $\sim 120 - 8000 M_{\odot}$).

5. Nearly 90% of these MCs are $\gtrsim 100$ pc from the plane. However, only 3% of MCs are in the $|z| \gtrsim 360$ pc region, suggesting that the high- z molecular gas is the disk population. Including the emission of the CO layer through the whole Galactic plane, the total molecular gas mass of the thick CO disk is estimated to be $8.5 \times 10^7 M_{\odot}$ in the range of $R_{GC} = 2-8.15$ kpc, which is about 10% of the total molecular mass in the same region of the inner Galaxy. The surface density and midplane mass density of the thick molecular gas disk are $\sim 0.4 M_{\odot}\text{pc}^{-2}$ and $\sim 0.0014 M_{\odot}\text{pc}^{-3}$ (or $\sim 0.02 \text{H}_2\text{cm}^{-3}$), respectively.

6. The cloud-cloud velocity dispersion of all tangent MCs seems to be smaller at larger R_{GC} , leading to a slope of $\sim -0.4 \text{ km s}^{-1}\text{kpc}^{-1}$ in the region of $R_{GC} = 2.2-6.4$ kpc. This value is about one-half of the HI gas when the joint gravitational potential is considered (Narayan & Jog 2002). The higher star formation rate at smaller R_{GC} is probably responsible for this feature.

7. Assuming the vertical equilibrium between the turbulent pressure of the molecular gas and the total gravitational force in the disk, we can use an exponential-disk

model of $\rho_0(R) = \rho_{GC}e^{-R/R_{sl}}$ to fit the distribution of the mass density in the Galactic midplane. The best-fit parameters are $R_{sl} = 3.2$ kpc and $\rho_{GC} = 1.28 M_{\odot}\text{pc}^{-3}$. The midplane mass density in the solar neighborhood is estimated to be $0.10 M_{\odot}\text{pc}^{-3}$ at $R_0 = 8.15$ kpc, which agrees with the local mass density of $0.097 \pm 0.013 M_{\odot}\text{pc}^{-3}$ suggested by McKee et al. (2015).

ACKNOWLEDGMENTS

We are grateful to all the members of the MWISP working group, particularly the staff members at the PMO-13.7m telescope, for their long-term support. We also thank the anonymous referee for providing many helpful comments and suggestions that largely improved the paper. MWISP was sponsored by National Key R&D Program of China with grant no. 2017YFA0402700 and CAS Key Research Program of Frontier Sciences with grant no. QYZDJ-SSW-SLH047. J.Y. and X.C. are supported by National Natural Science Foundation of China through grant 12041305. Y.S. is supported by the Youth Innovation Promotion Association, CAS (2018355). This work is supported by NSFC 11629302, 11773077, and 11803091.

Facility: PMO 13.7m

Software: GILDAS/CLASS (Pety 2005)

REFERENCES

- Benedettini, M., Molinari, S., Baldeschi, A., et al. 2020, A&A, 633, A147, doi: [10.1051/0004-6361/201936096](https://doi.org/10.1051/0004-6361/201936096)
- Bland-Hawthorn, J., & Gerhard, O. 2016, ARA&A, 54, 529, doi: [10.1146/annurev-astro-081915-023441](https://doi.org/10.1146/annurev-astro-081915-023441)
- Blitz, L., Magnani, L., & Mundy, L. 1984, ApJL, 282, L9, doi: [10.1086/184293](https://doi.org/10.1086/184293)
- Bolatto, A. D., Wolfire, M., & Leroy, A. K. 2013, ARA&A, 51, 207, doi: [10.1146/annurev-astro-082812-140944](https://doi.org/10.1146/annurev-astro-082812-140944)
- Bregman, J. N. 1980, ApJ, 236, 577, doi: [10.1086/157776](https://doi.org/10.1086/157776)
- Bronfman, L., Cohen, R. S., Alvarez, H., May, J., & Thaddeus, P. 1988, ApJ, 324, 248, doi: [10.1086/165892](https://doi.org/10.1086/165892)
- Caldú-Primo, A., Schrubba, A., Walter, F., et al. 2013, AJ, 146, 150, doi: [10.1088/0004-6256/146/6/150](https://doi.org/10.1088/0004-6256/146/6/150)
- Clemens, D. P. 1985, ApJ, 295, 422, doi: [10.1086/163386](https://doi.org/10.1086/163386)

- Clemens, D. P., Sanders, D. B., & Scoville, N. Z. 1988, *ApJ*, 327, 139, doi: [10.1086/166177](https://doi.org/10.1086/166177)
- Colombo, D., Rosolowsky, E., Duarte-Cabral, A., et al. 2019, *MNRAS*, 483, 4291, doi: [10.1093/mnras/sty3283](https://doi.org/10.1093/mnras/sty3283)
- Combes, F. 1991, *ARA&A*, 29, 195, doi: [10.1146/annurev.aa.29.090191.001211](https://doi.org/10.1146/annurev.aa.29.090191.001211)
- Dame, T. M., Hartmann, D., & Thaddeus, P. 2001, *ApJ*, 547, 792, doi: [10.1086/318388](https://doi.org/10.1086/318388)
- Dame, T. M., & Thaddeus, P. 1994, *ApJL*, 436, L173, doi: [10.1086/187660](https://doi.org/10.1086/187660)
- . 2008, *ApJL*, 683, L143, doi: [10.1086/591669](https://doi.org/10.1086/591669)
- . 2011, *ApJL*, 734, L24, doi: [10.1088/2041-8205/734/1/L24](https://doi.org/10.1088/2041-8205/734/1/L24)
- di Teodoro, E. M., McClure-Griffiths, N. M., Lockman, F. J., & Armillotta, L. 2020, *Nature*, 584, 364. <https://arxiv.org/abs/2008.09121>
- Dickey, J. M., & Lockman, F. J. 1990, *ARA&A*, 28, 215, doi: [10.1146/annurev.aa.28.090190.001243](https://doi.org/10.1146/annurev.aa.28.090190.001243)
- Du, X., Xu, Y., Yang, J., & Sun, Y. 2017, *ApJS*, 229, 24, doi: [10.3847/1538-4365/aa5d9d](https://doi.org/10.3847/1538-4365/aa5d9d)
- Du, X., Xu, Y., Yang, J., et al. 2016, *ApJS*, 224, 7, doi: [10.3847/0067-0049/224/1/7](https://doi.org/10.3847/0067-0049/224/1/7)
- Eden, D. J., Moore, T. J. T., Currie, M. J., et al. 2020, *MNRAS*, 498, 5936, doi: [10.1093/mnras/staa2734](https://doi.org/10.1093/mnras/staa2734)
- Ford, H. A., Lockman, F. J., & McClure-Griffiths, N. M. 2010, *ApJ*, 722, 367, doi: [10.1088/0004-637X/722/1/367](https://doi.org/10.1088/0004-637X/722/1/367)
- Ford, H. A., McClure-Griffiths, N. M., Lockman, F. J., et al. 2008, *ApJ*, 688, 290, doi: [10.1086/592188](https://doi.org/10.1086/592188)
- Garcia-Burillo, S., Guelin, M., Cernicharo, J., & Dahlem, M. 1992, *A&A*, 266, 21
- Heyer, M., & Dame, T. M. 2015, *ARA&A*, 53, 583, doi: [10.1146/annurev-astro-082214-122324](https://doi.org/10.1146/annurev-astro-082214-122324)
- Houck, J. C., & Bregman, J. N. 1990, *ApJ*, 352, 506, doi: [10.1086/168554](https://doi.org/10.1086/168554)
- Iwasaki, K., Tomida, K., Inoue, T., & Inutsuka, S.-i. 2019, *ApJ*, 873, 6, doi: [10.3847/1538-4357/ab02ff](https://doi.org/10.3847/1538-4357/ab02ff)
- Krumholz, M. R., Burkhart, B., Forbes, J. C., & Crocker, R. M. 2018, *MNRAS*, 477, 2716, doi: [10.1093/mnras/sty852](https://doi.org/10.1093/mnras/sty852)
- Langer, W. D., Pineda, J. L., & Velusamy, T. 2014, *A&A*, 564, A101, doi: [10.1051/0004-6361/201323281](https://doi.org/10.1051/0004-6361/201323281)
- Lockman, F. J. 1984, *ApJ*, 283, 90, doi: [10.1086/162277](https://doi.org/10.1086/162277)
- . 2002, *ApJL*, 580, L47, doi: [10.1086/345495](https://doi.org/10.1086/345495)
- Lockman, F. J., & Gehman, C. S. 1991, *ApJ*, 382, 182, doi: [10.1086/170706](https://doi.org/10.1086/170706)
- Malhotra, S. 1994a, *ApJ*, 437, 194, doi: [10.1086/174988](https://doi.org/10.1086/174988)
- . 1994b, *ApJ*, 433, 687, doi: [10.1086/174677](https://doi.org/10.1086/174677)
- . 1995, *ApJ*, 448, 138, doi: [10.1086/175946](https://doi.org/10.1086/175946)
- McClure-Griffiths, N. M., & Dickey, J. M. 2016, *ApJ*, 831, 124, doi: [10.3847/0004-637X/831/2/124](https://doi.org/10.3847/0004-637X/831/2/124)
- McKee, C. F., Parravano, A., & Hollenbach, D. J. 2015, *ApJ*, 814, 13, doi: [10.1088/0004-637X/814/1/13](https://doi.org/10.1088/0004-637X/814/1/13)
- Nakanishi, H., & Sofue, Y. 2006, *PASJ*, 58, 847, doi: [10.1093/pasj/58.5.847](https://doi.org/10.1093/pasj/58.5.847)
- Narayan, C. A., & Jog, C. J. 2002, *A&A*, 394, 89, doi: [10.1051/0004-6361:20021128](https://doi.org/10.1051/0004-6361:20021128)
- Peek, J. E. G., Heiles, C., Douglas, K. A., et al. 2011, *ApJS*, 194, 20, doi: [10.1088/0067-0049/194/2/20](https://doi.org/10.1088/0067-0049/194/2/20)
- Peek, J. E. G., Babler, B. L., Zheng, Y., et al. 2018, *ApJS*, 234, 2, doi: [10.3847/1538-4365/aa91d3](https://doi.org/10.3847/1538-4365/aa91d3)
- Pety, J. 2005, in *SF2A-2005: Semaine de l'Astrophysique Francaise*, ed. F. Casoli, T. Contini, J. M. Hameury, & L. Pagani, (Les Ulis: EDP), 721
- Pety, J., Schinnerer, E., Leroy, A. K., et al. 2013, *ApJ*, 779, 43, doi: [10.1088/0004-637X/779/1/43](https://doi.org/10.1088/0004-637X/779/1/43)
- Putman, M. E., Peek, J. E. G., & Joung, M. R. 2012, *ARA&A*, 50, 491, doi: [10.1146/annurev-astro-081811-125612](https://doi.org/10.1146/annurev-astro-081811-125612)
- Reid, M. J., Dame, T. M., Menten, K. M., & Brunthaler, A. 2016, *ApJ*, 823, 77, doi: [10.3847/0004-637X/823/2/77](https://doi.org/10.3847/0004-637X/823/2/77)
- Reid, M. J., Menten, K. M., Brunthaler, A., et al. 2019, *ApJ*, 885, 131, doi: [10.3847/1538-4357/ab4a11](https://doi.org/10.3847/1538-4357/ab4a11)
- Rice, T. S., Goodman, A. A., Bergin, E. A., Beaumont, C., & Dame, T. M. 2016, *ApJ*, 822, 52, doi: [10.3847/0004-637X/822/1/52](https://doi.org/10.3847/0004-637X/822/1/52)
- Rigby, A. J., Moore, T. J. T., Plume, R., et al. 2016, *MNRAS*, 456, 2885, doi: [10.1093/mnras/stv2808](https://doi.org/10.1093/mnras/stv2808)
- Roman-Duval, J., Jackson, J. M., Heyer, M., Rathborne, J., & Simon, R. 2010, *ApJ*, 723, 492, doi: [10.1088/0004-637X/723/1/492](https://doi.org/10.1088/0004-637X/723/1/492)
- Sanders, D. B., Solomon, P. M., & Scoville, N. Z. 1984, *ApJ*, 276, 182, doi: [10.1086/161602](https://doi.org/10.1086/161602)

- Schuller, F., Csengeri, T., Urquhart, J. S., et al. 2017, *A&A*, 601, A124, doi: [10.1051/0004-6361/201628933](https://doi.org/10.1051/0004-6361/201628933)
- Schuller, F., Urquhart, J. S., Csengeri, T., et al. 2021, *MNRAS*, 500, 3064, doi: [10.1093/mnras/staa2369](https://doi.org/10.1093/mnras/staa2369)
- Shan, W., Yang, J., Shi, S., et al. 2012, *ITTST*, 2, 593, doi: [10.1109/TTHZ.2012.2213818](https://doi.org/10.1109/TTHZ.2012.2213818)
- Shapiro, P. R., & Field, G. B. 1976, *ApJ*, 205, 762, doi: [10.1086/154332](https://doi.org/10.1086/154332)
- Sofue, Y., Kohno, M., Torii, K., et al. 2019, *PASJ*, 71, S1, doi: [10.1093/pasj/psy094](https://doi.org/10.1093/pasj/psy094)
- Soler, J. D., Beuther, H., Syed, J., et al. 2020, *A&A*, 642, A163, doi: [10.1051/0004-6361/202038882](https://doi.org/10.1051/0004-6361/202038882)
- Spitoni, E., Recchi, S., & Matteucci, F. 2008, *A&A*, 484, 743, doi: [10.1051/0004-6361:200809403](https://doi.org/10.1051/0004-6361:200809403)
- Stark, A. A. 1984, *ApJ*, 281, 624, doi: [10.1086/162137](https://doi.org/10.1086/162137)
- Stark, A. A., & Brand, J. 1989, *ApJ*, 339, 763, doi: [10.1086/167334](https://doi.org/10.1086/167334)
- Su, Y., Sun, Y., Li, C., et al. 2016, *ApJ*, 828, 59, doi: [10.3847/0004-637X/828/1/59](https://doi.org/10.3847/0004-637X/828/1/59)
- Su, Y., Zhou, X., Yang, J., et al. 2018, *ApJ*, 863, 103, doi: [10.3847/1538-4357/aad04e](https://doi.org/10.3847/1538-4357/aad04e)
- Su, Y., Yang, J., Zhang, S., et al. 2019, *ApJS*, 240, 9, doi: [10.3847/1538-4365/aaf1c8](https://doi.org/10.3847/1538-4365/aaf1c8)
- Sun, J. X., Lu, D. R., Yang, J., et al. 2018, *AcASn*, 59, 3
- Sun, Y., Su, Y., Zhang, S.-B., et al. 2017, *ApJS*, 230, 17, doi: [10.3847/1538-4365/aa63ea](https://doi.org/10.3847/1538-4365/aa63ea)
- Sun, Y., Xu, Y., Yang, J., et al. 2015, *ApJL*, 798, L27, doi: [10.1088/2041-8205/798/2/L27](https://doi.org/10.1088/2041-8205/798/2/L27)
- Sun, Y., Yang, J., Xu, Y., et al. 2020, *ApJS*, 246, 7, doi: [10.3847/1538-4365/ab5b97](https://doi.org/10.3847/1538-4365/ab5b97)
- Torii, K., Fujita, S., Nishimura, A., et al. 2019, *PASJ*, 71, S2, doi: [10.1093/pasj/psz033](https://doi.org/10.1093/pasj/psz033)
- Vallée, J. P. 2014, *ApJS*, 215, 1, doi: [10.1088/0067-0049/215/1/1](https://doi.org/10.1088/0067-0049/215/1/1)
- Velusamy, T., & Langer, W. D. 2014, *A&A*, 572, A45, doi: [10.1051/0004-6361/201424350](https://doi.org/10.1051/0004-6361/201424350)
- Yan, Q.-Z., Yang, J., Su, Y., Sun, Y., & Wang, C. 2020, *ApJ*, 898, 80, doi: [10.3847/1538-4357/ab9f9c](https://doi.org/10.3847/1538-4357/ab9f9c)

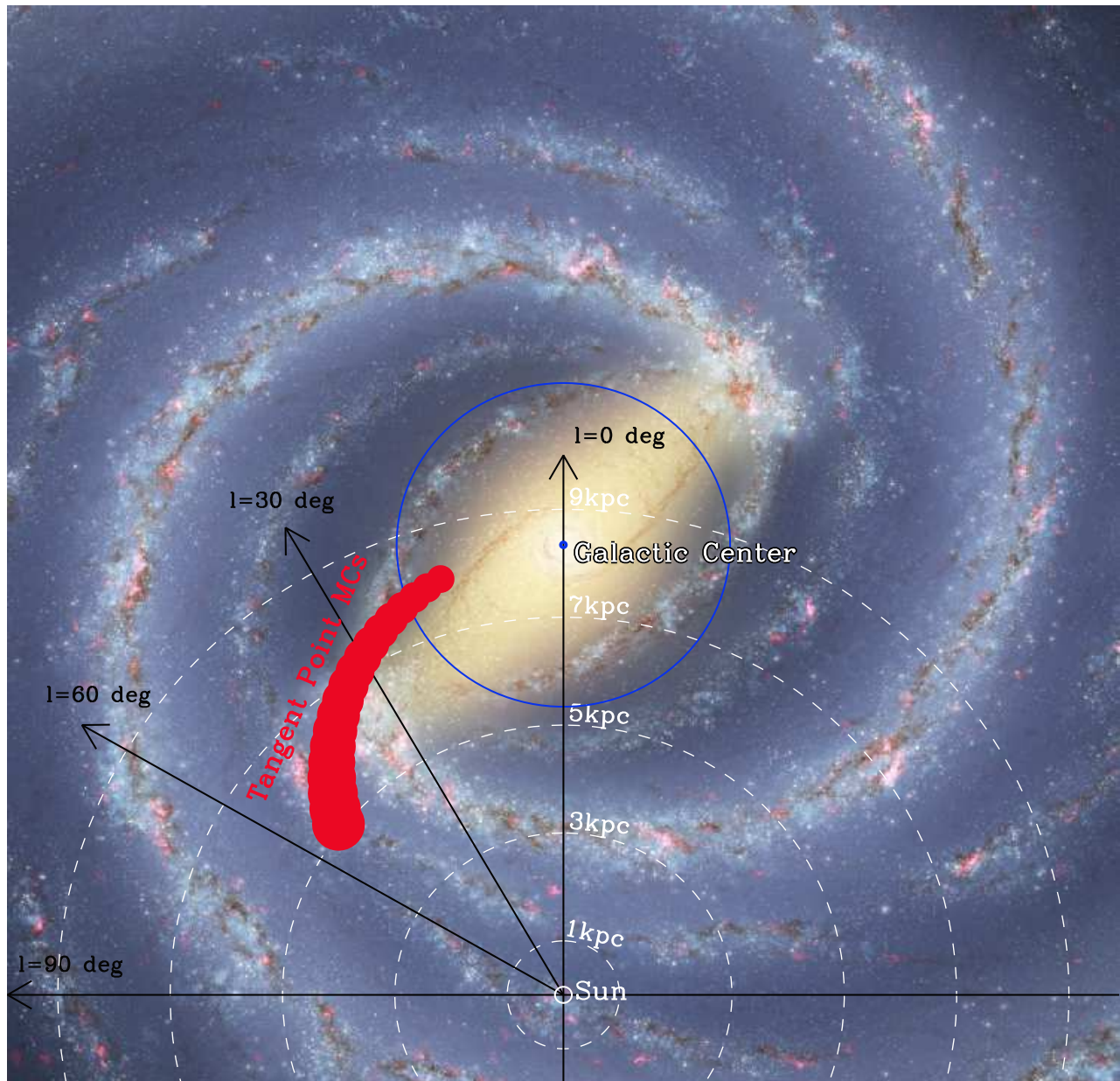


Figure 1. Face-on view of the Milky Way (R. Hurt: NASA/JPL-Caltech/SSC) superposed on the tangent-point molecular gas of the Galaxy. The MCs near the tangent points are identified based on the MWISP CO data toward the longitude range of 16° – 52° (or a red belt with a length of ~ 5.1 kpc). Note that the width of the belt in the map is proportional to the longitude, and the mean width is about 500 pc based on the model (e.g., Lockman 1984). The Sun at $[0, -8.15]$ kpc and the Galactic center at $[0, 0]$ kpc are also labeled on the map. The blue circle indicates the 3 kpc ring with respect to the Galactic center.

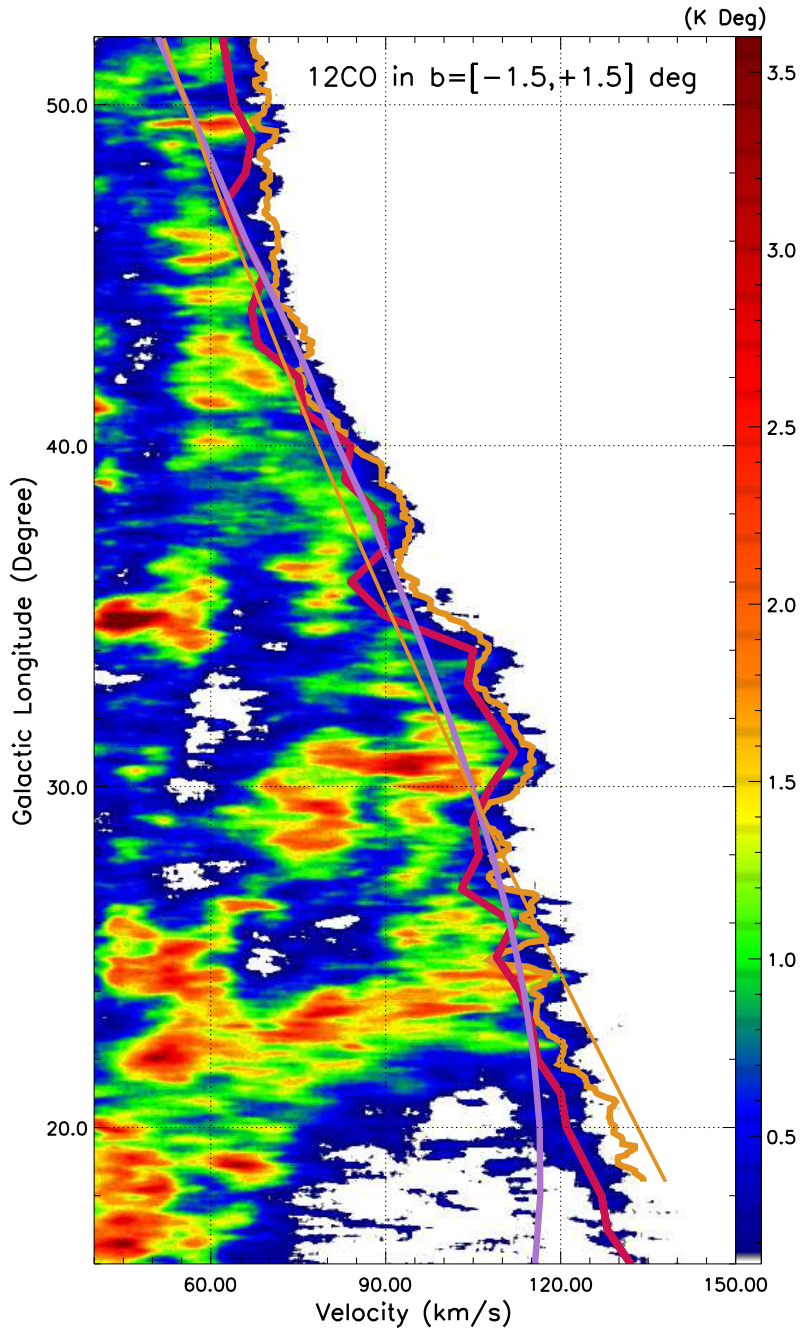


Figure 2. Longitude–velocity diagram of the ^{12}CO emission for the molecular gas along $l = 16^\circ - 52^\circ$. The region has a width of $3^\circ 0$, i.e., $b = [-1^\circ 5, 1^\circ 5]$. The red line indicates the terminal velocity for the tangent-point gas (V_{tan}) based on the MWISP CO data. The purple and golden lines show the rotation curve from Reid et al. (2019) and the HI result (the thick line for the measured values and the thin line for the linear fit) from McClure-Griffiths & Dickey (2016), respectively.

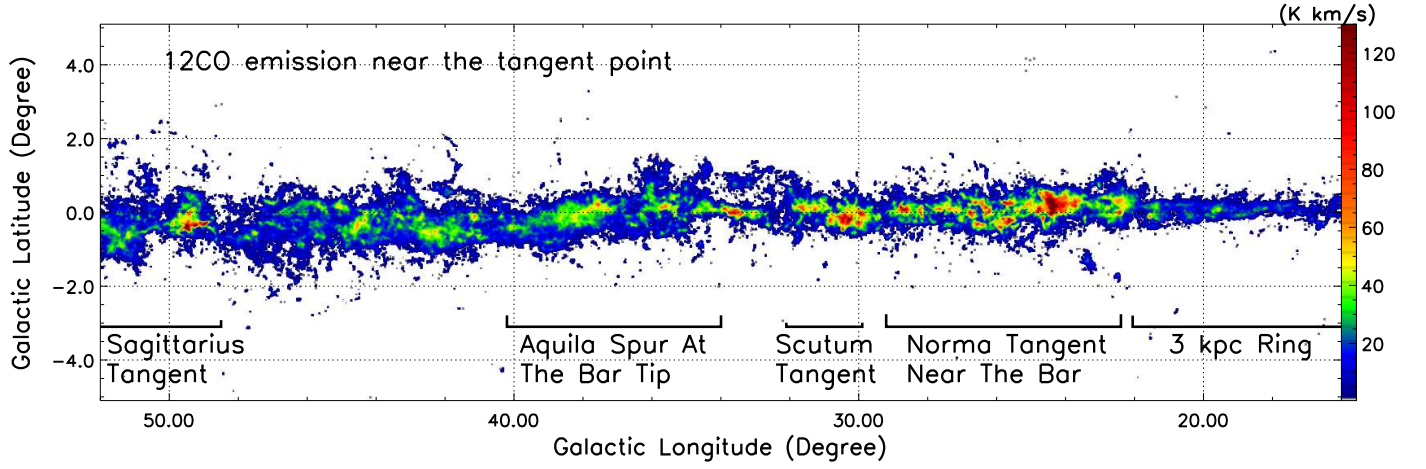


Figure 3. ^{12}CO ($J=1-0$) intensity map toward $l = 16^\circ - 52^\circ$ in the velocity range of $V(l) \gtrsim V_{\text{tan}}(l) - 7 \text{ km s}^{-1}$. The tangent velocity, i.e., $V_{\text{tan}}(l)$, is well determined from the red line in Figure 2. Some large-scale structures seen in the longitude–velocity diagram (Figure 2) are also labeled on the map of the integrated CO emission near the tangent points (e.g., see Vallée 2014; Reid et al. 2016).

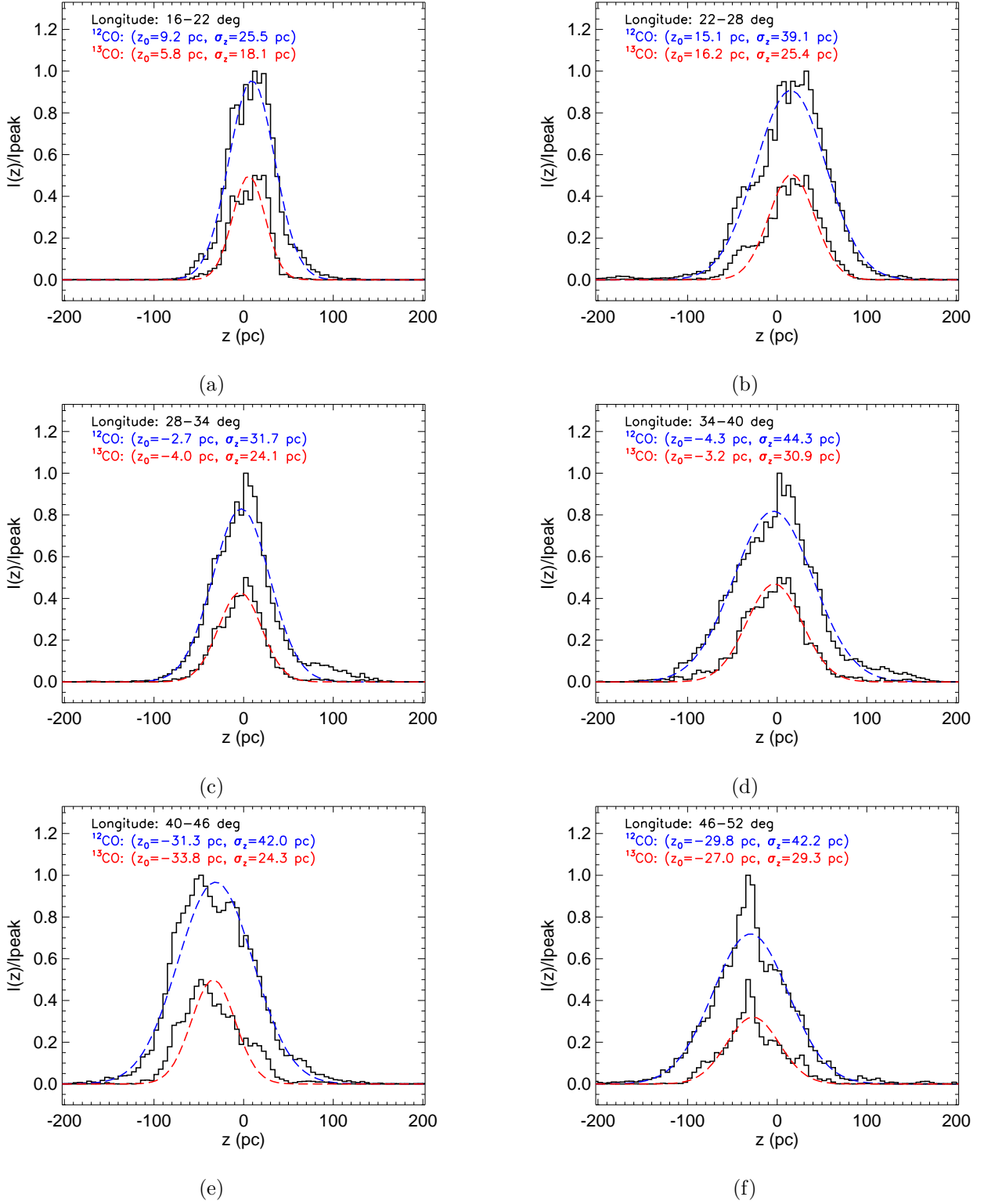


Figure 4. (a)–(f) Vertical distribution of the total integrated ^{12}CO (black solid line) and ^{13}CO (black solid line, scale to 0.5) intensity toward the longitude range of $16^\circ - 22^\circ$, $22^\circ - 28^\circ$, $28^\circ - 34^\circ$, $34^\circ - 40^\circ$, $40^\circ - 46^\circ$, and $46^\circ - 52^\circ$, respectively. The bin in each panel is 5 pc, which corresponds to about 5 pixels (2.5) at a distance of ~ 7 kpc. The blue dashed line indicates the Gaussian fit of the vertical distribution for the Galactic thin disk based on the MWISP ^{12}CO emission, while the red dashed line is for the ^{13}CO gas. The fitted parameters of z_0 and σ_z (i.e., $\text{FWHM} = 2.355 \times \sigma_z$) are also labeled on each panel for the one Gaussian component.

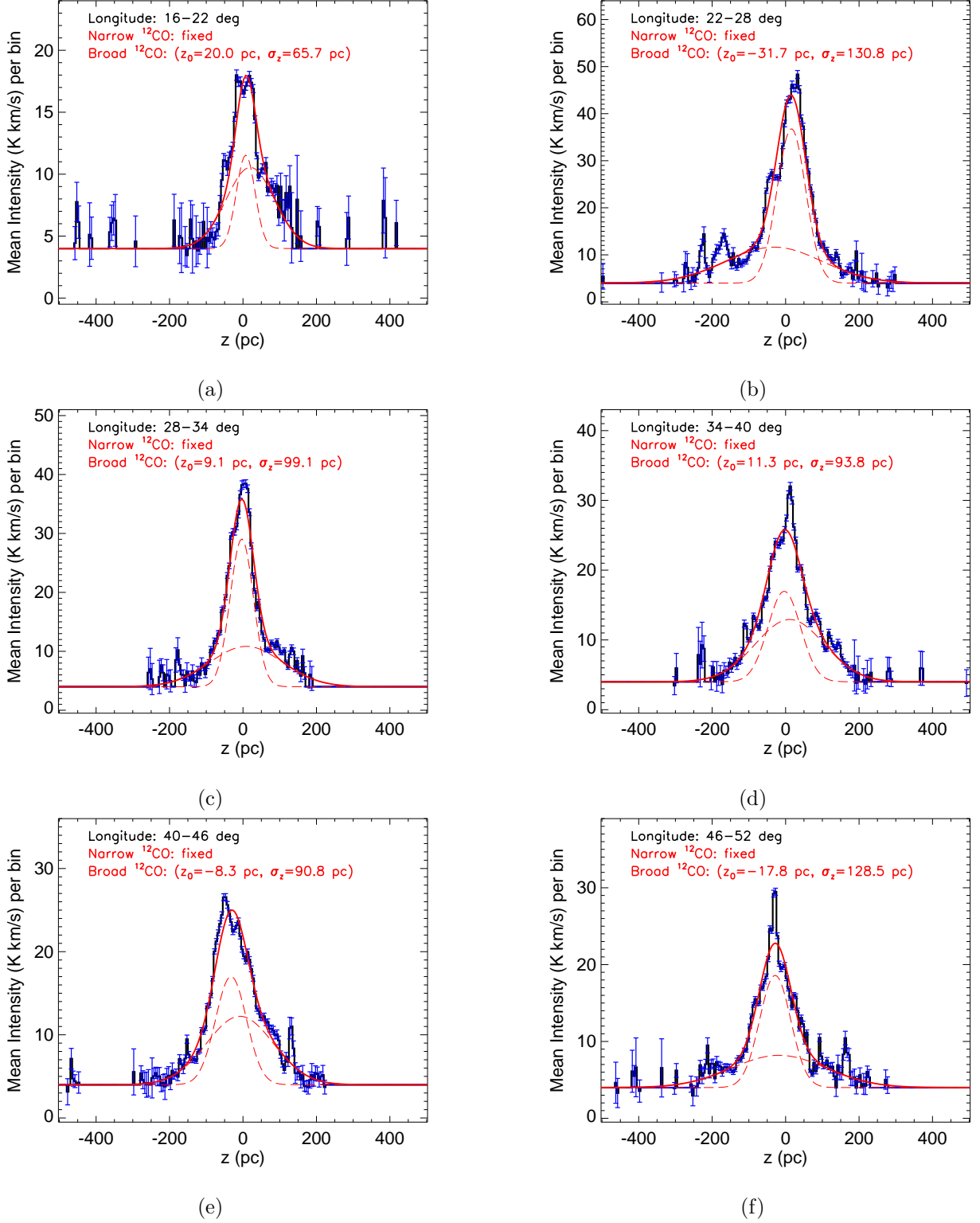


Figure 5. (a)–(f) Vertical distribution of the mean intensity (i.e., the black solid line for $I_{\text{total}}/\sqrt{N_{\text{pixel}}}$, see the text) of the ^{12}CO emission toward the longitude range of $16^\circ - 22^\circ$, $22^\circ - 28^\circ$, $28^\circ - 34^\circ$, $34^\circ - 40^\circ$, $40^\circ - 46^\circ$, and $46^\circ - 52^\circ$, respectively. The bin in each panel is 5 pc. We assume $\sqrt{N_{\text{pixel}}}$ errors for each bin. The solid red line displays the best fit of two Gaussian components (i.e., the fixed narrow dashed line from Figure 4 + the fitted broad dashed line) for the ^{12}CO gas. The fitted parameters of z_0 and σ_z (i.e., $\text{FWHM}=2.355 \times \sigma_z$) are also labeled in each panel for the broad Gaussian component. Note that the zero point of the fitting is roughly 4 K km s^{-1} , which is $\sim 3I_{\text{rms}}$ of the integrated CO intensity near the tangent points.

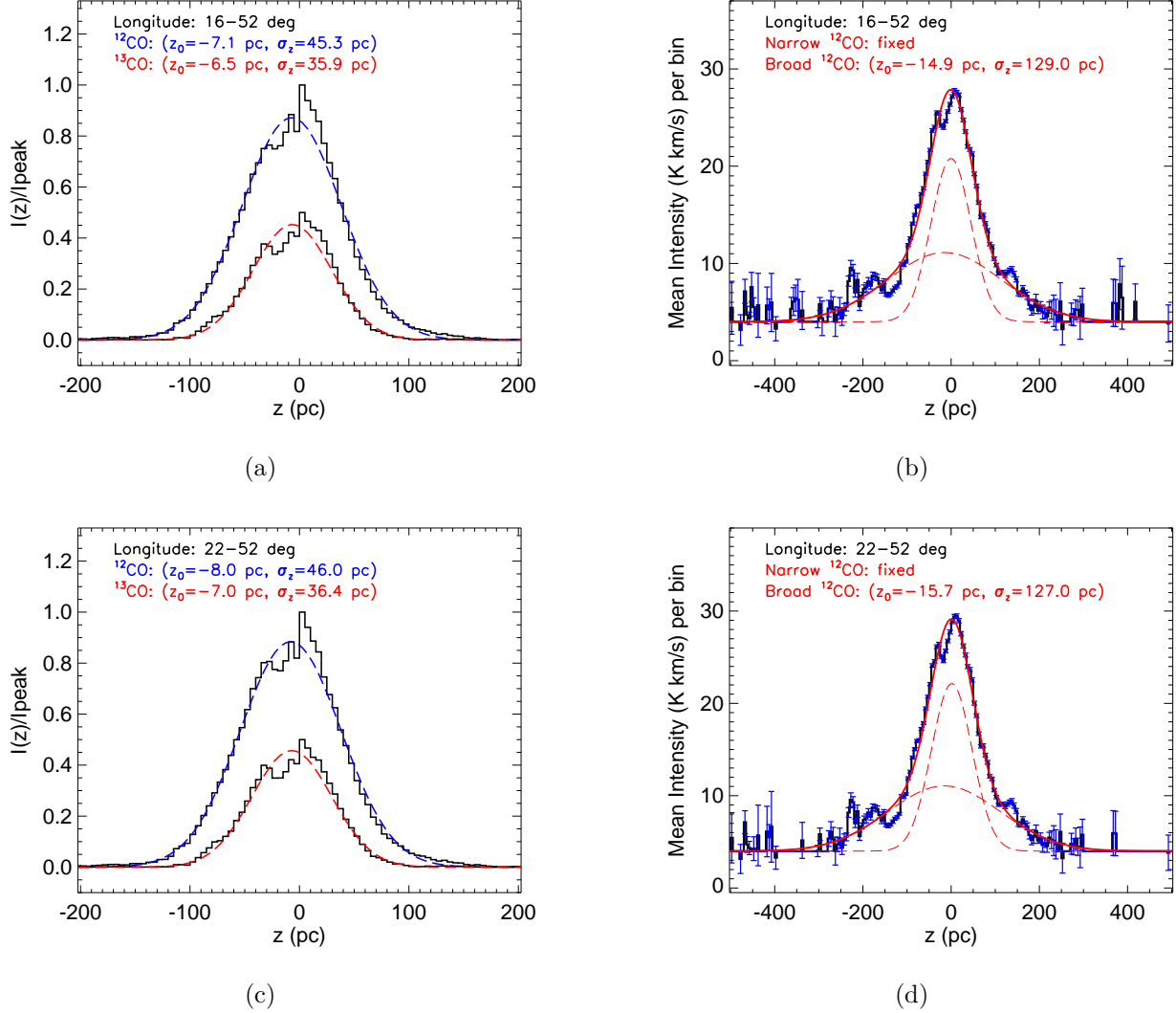


Figure 6. Left panels: same as Figure 4 but for the longitude range of $16^\circ - 52^\circ$ and $22^\circ - 52^\circ$ based on the total integrated CO emission. The fitted parameters of the ^{12}CO emission for the thin disk are used to fix the narrow Gaussian component in the right panels. Right panels: same as Figure 5 but for the longitude range of $16^\circ - 52^\circ$ and $22^\circ - 52^\circ$ based on the mean intensity of the ^{12}CO emission. The fitted parameters of z_0 and σ_z (i.e., $\text{FWHM} = 2.355 \times \sigma_z$) are labeled in each panel for the broad Gaussian component (i.e., the thick CO disk).

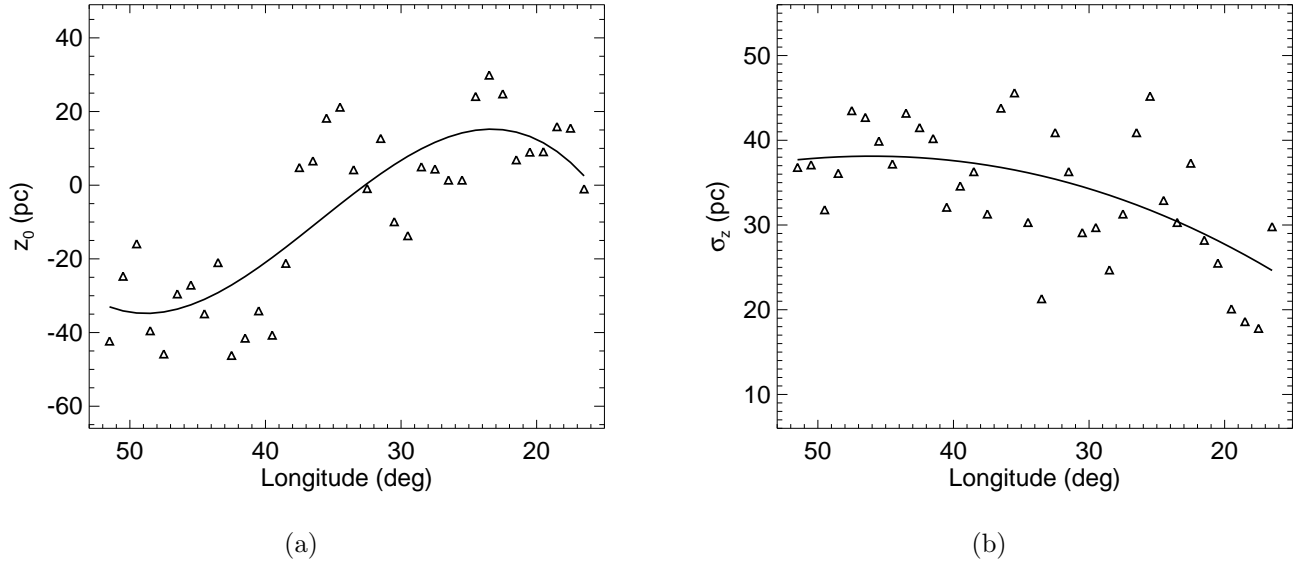


Figure 7. The position of the centroid of the molecular gas near the tangent points (z_0 in the left panel) and the scale height of the thin gas disk (σ_z in the right panel) based on the ^{12}CO emission at different Galactic longitudes of $l = 16^\circ - 52^\circ$ with a separation of 1° . The line indicates the least-square fit from a third-order polynomial by using the 36 points.

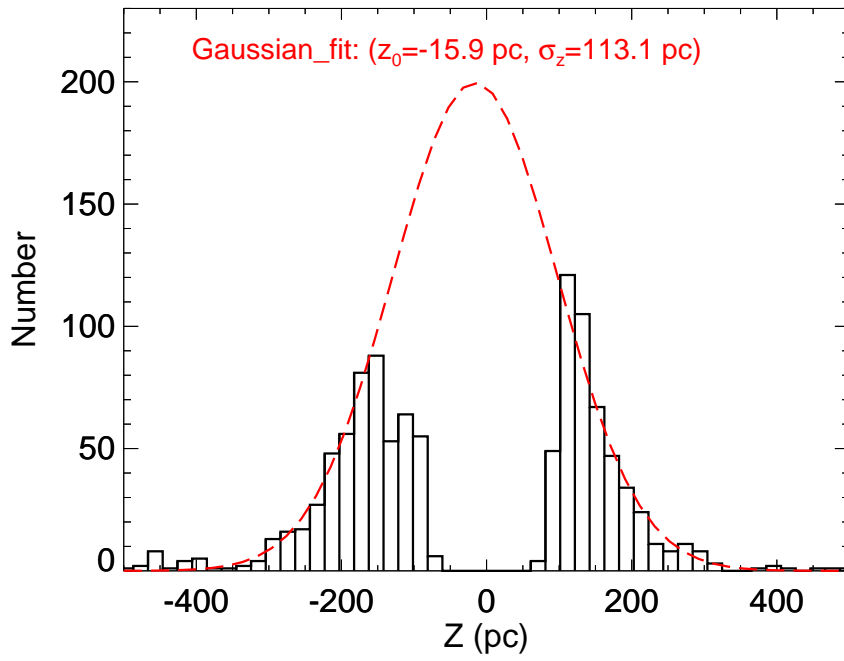


Figure 8. Vertical distribution of the identified MCs far from the Galactic plane. The red dashed line shows the Gaussian fit for the broad component of the Galactic thick disk.

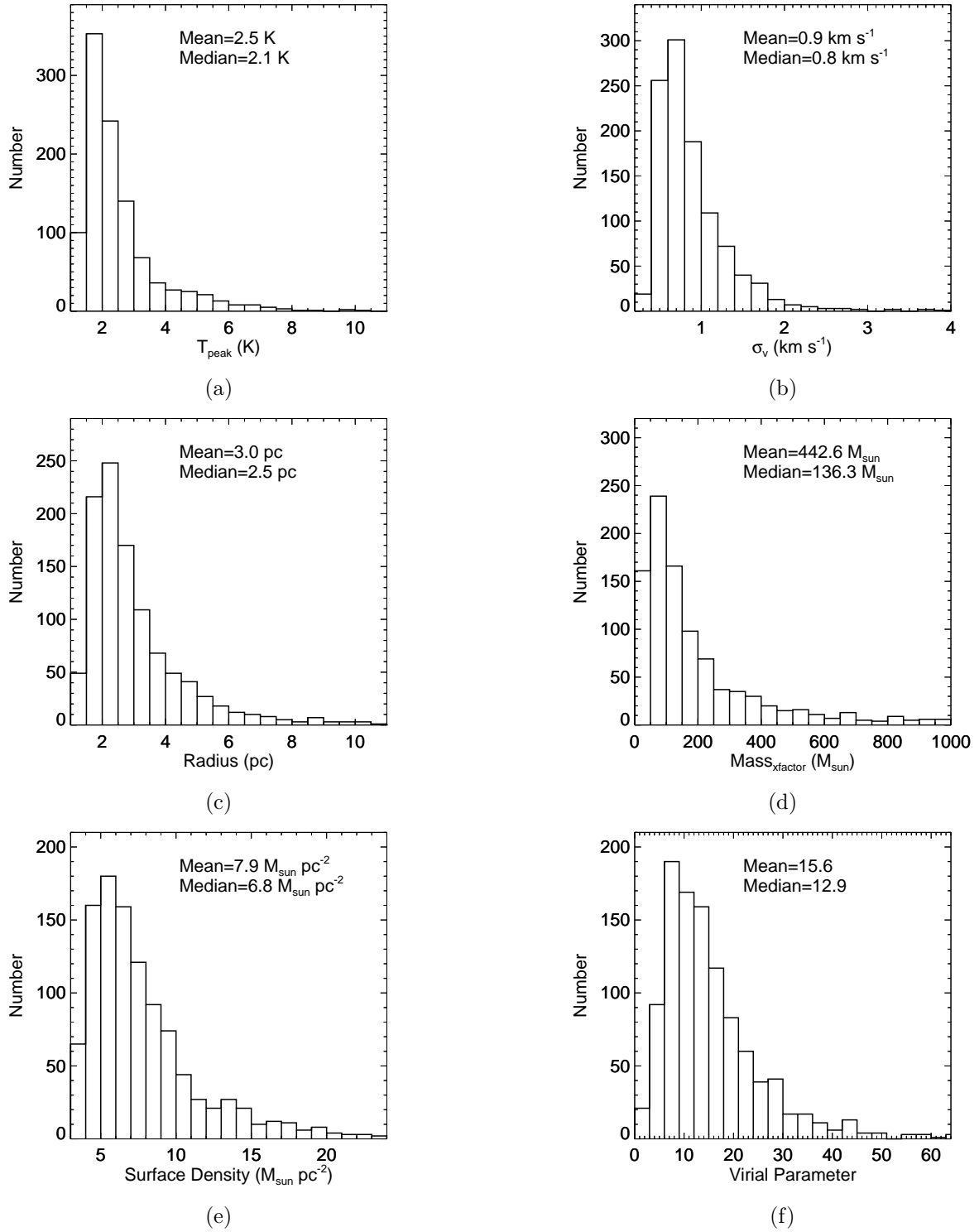


Figure 9. (a)–(f) Histogram of the peak temperature, the velocity dispersion, the radius, the mass, the surface density, and the virial parameter of the ^{12}CO cloud far from the Galactic plane.

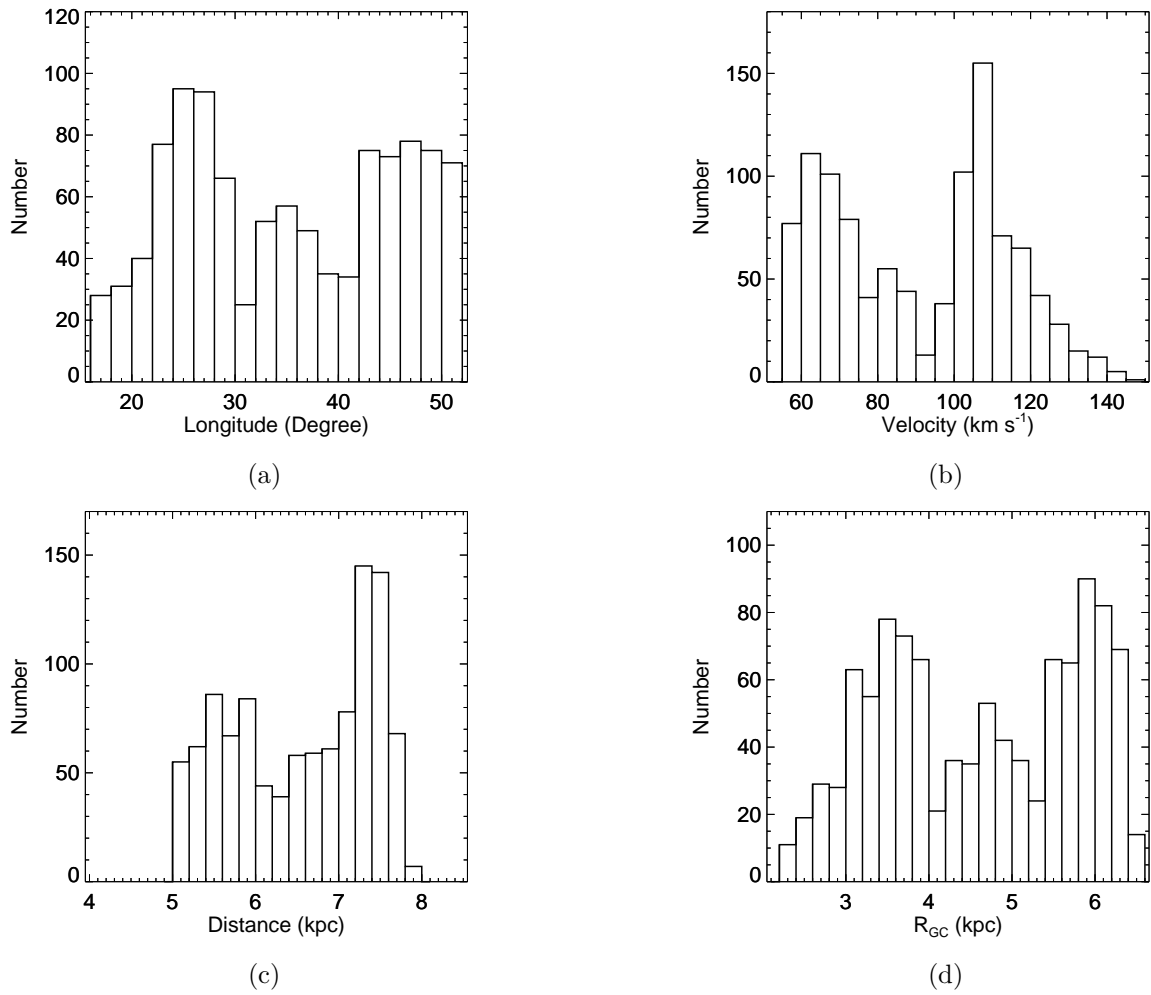


Figure 10. (a)–(d) Longitude, velocity, distance, and Galactocentric distance distributions of the MCs far from the Galactic plane.

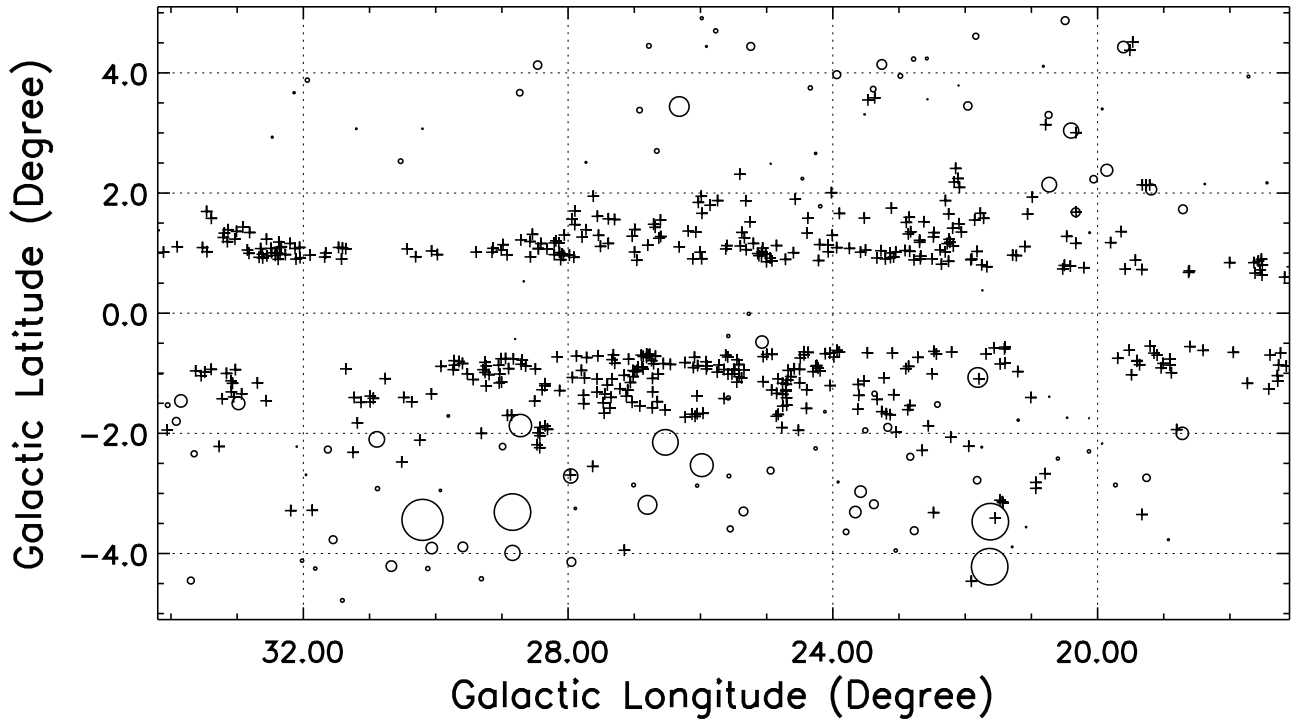


Figure 11. Comparison between the high- z CO clouds (crosses with the uniform size; this paper) and the disk-halo HI clouds (circles; Ford et al. 2010). Note that the circle's size is not the true angular size of the HI clouds, but it is proportional to the mass of the HI clouds.

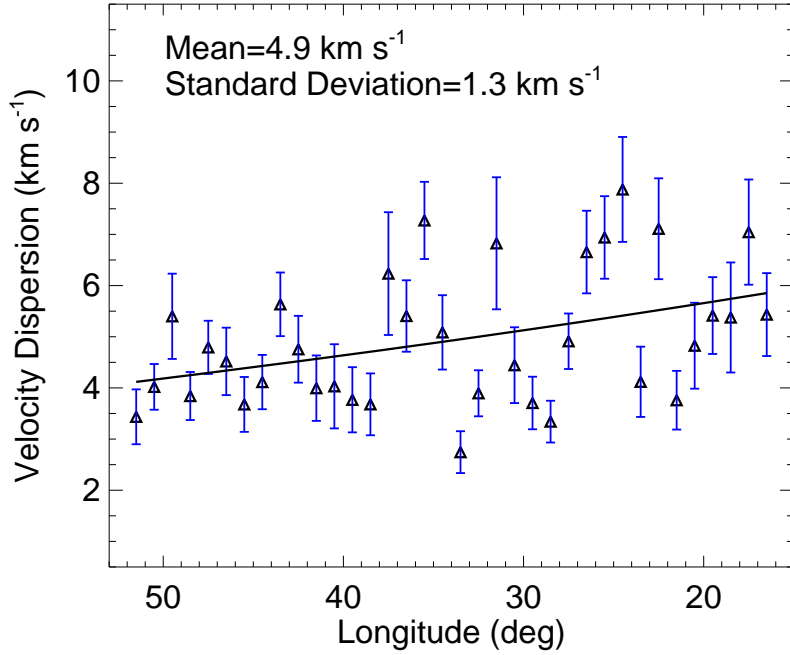


Figure 12. Cloud-cloud velocity dispersion (σ_{cc}) for all MCs (i.e., the thin + thick CO disk) near the tangent points toward $l = 16^\circ - 52^\circ$. The line indicates the least-squares fit from a third-order polynomial (nearly linear form with a slope of $\sim -0.4 \text{ km s}^{-1} \text{ kpc}^{-1}$) by using the current data of $R_{GC} \sim 2.2\text{--}6.4 \text{ kpc}$. The error for each bin of 1° is assumed as $\sigma_{cc}/\sqrt{N_{\text{cloud}}}$. The mean value of σ_{cc} and its standard deviation are also labeled on the panel.

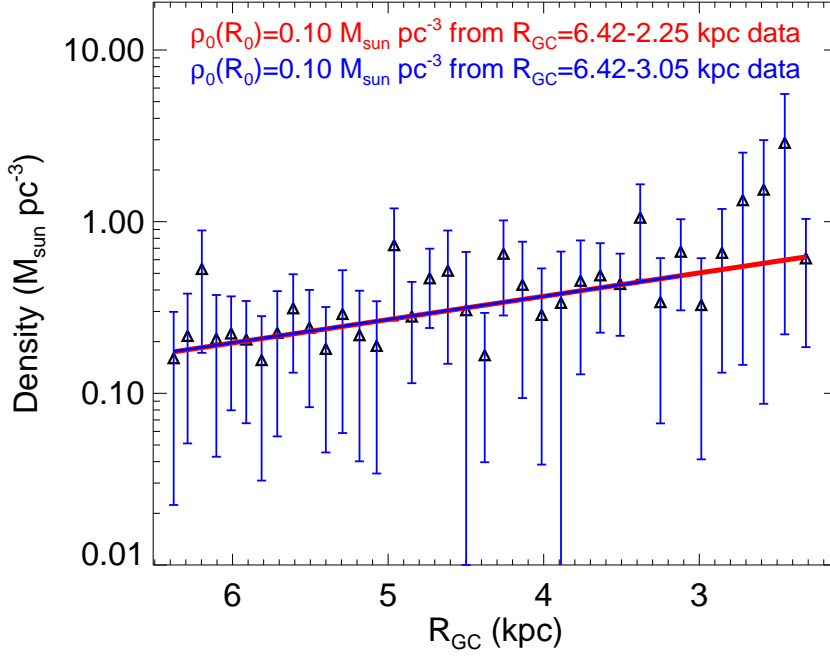


Figure 13. Midplane mass density for different Galactocentric distances (R_{GC}) derived from the CO scale height (Figure 7b) and the velocity dispersion (Figure 12). The line shows the exponential-disk model of $\rho_0(R) = \rho_{GC}e^{-R/R_{s1}}$, where the fitted mass density at the Galactic center $\rho_{GC} = 1.28 M_{\odot} \text{pc}^{-3}$, and the scale length, $R_{s1} = 3.20 \text{ kpc}$. The midplane mass density at the Sun ($R_{GC} = R_0 = 8.15 \text{ kpc}$) is estimated to be $\sim 0.10 M_{\odot} \text{pc}^{-3}$.

Table 1. Parameters of 1055 Molecular Clouds Far from the Galactic Plane based on the MWISP $^{12}\text{CO}(J=1-0)$ Emission

ID	l	b	V_{LSR}	σ_v	T_{peak}	Area	Distance ^a	z scale	Mass	α^b
	($^\circ$)	($^\circ$)	(km s^{-1})	(km s^{-1})	(K)	(arcmin^2)	(kpc)	(pc)	(M_\odot)	
(1)	(2)	(3)	(4)	(5)	(6)	(7)	(8)	(9)	(10)	(11)
1	16.103	0.896	143.16	2.07	1.84	10.75	7.8	122.5	690	31.5
2	16.278	0.976	137.99	1.00	1.29	2.50	7.8	133.2	100	24.2
3	16.436	-0.770	128.18	0.85	1.97	5.00	7.8	-105.0	160	15.4
4	16.498	0.809	130.07	1.31	2.60	14.25	7.8	110.4	620	15.9
5	16.526	0.929	139.87	3.27	2.54	15.75	7.8	126.7	1160	56.4
6	16.768	-0.600	128.00	1.37	3.30	31.50	7.8	-81.8	1700	9.5
7	16.801	-1.173	128.58	0.77	1.70	6.50	7.8	-159.8	220	10.5

NOTE— ^a The error of the estimated distance is about 2%–20% from $l = 16^\circ - 52^\circ$ assuming that the MCs are located near tangent points with a velocity uncertainty of $\sim 5 \text{ km s}^{-1}$ along the line of sight (e.g., refer to the A5 model in Reid et al. 2019). ^b The MC’s virial parameter estimated from the definition of $\alpha = \frac{5\sigma_v^2 R}{GM_{\text{Xfactor}}}$ (see Section 3.3.1).

Table 2. Statistical Properties of the high- z Molecular Clouds^a

Median						Mean		
T_{peak}	Radius	σ_v	Mass	Surface Density	α^b	σ_{cc}	Thickness	γ^c
(K)	(pc)	(km s^{-1})	(M_\odot)	($M_\odot \text{ pc}^{-2}$)		(km s^{-1})	(pc)	
2.1	2.5	0.8	136.3	6.8	12.9	$\sim 4.4\text{--}5.6$	~ 280	-1.74

NOTE— ^a The properties of the molecular gas indicate that the high- z MCs belong to a new disk population that was not discovered by previous CO observations due to the low sensitivity, low resolution, and/or limited latitude coverage. ^b α is the virial parameter of the MCs (see the text). ^c γ is the spectral index of the mass distribution of the high- z MCs with the form $\frac{dN}{dM} \propto M^\gamma$ in the MC’s mass range of $\sim 120 - 8000 M_\odot$.

Table 3. Thickness of the Inner Galaxy Traced by Different Tracers

Tracer	FWHM ^a	References ^b	Comments
CO	~85 pc	1,2	The well-known thin molecular gas disk
	~280 pc	1	The thick disk is composed of many discrete MCS with small size and low mass
C II	~120 pc	3	C II with bright CO emission as the dense H ₂ gas (the overestimated thin CO disk)
	~190 pc	3	Bright diffuse C II emission as the CO-faint diffuse H ₂ gas
	~320 pc	3	Faint diffuse C II emission as the diffuse H I and WIM gas
H I	~230 pc	4,5	The narrow Gaussian component for the cold neutral medium
	~540 pc	4,5	The broad Gaussian component for the warm neutral medium
	~1300-1600 pc	5,6	The exponential component for the warm neutral medium (the disk-halo gas)

NOTE— ^a The estimated thickness has been scaled to $R_0 = 8.15$ kpc (e.g., Reid et al. 2019). ^b 1. This paper, 2. Malhotra (1994b), 3. Velusamy & Langer (2014), 4. Dickey & Lockman (1990), 5. Lockman & Gehman (1991), 6. Ford et al. (2010).